# Chapter 2
# Extraordinary Optical Transmission

## 2.1 Introduction

Anyone of us has experimented that light spreads in all directions upon interacting with objects. Another matter is how it does it. Diffraction theory is an old problem in optics, which goes back the works by Thomas Young and Augustin-Jean Fresnel in the nineteenth century. In 1944 an important landmark in that widely studied topic was put on the map by Hans Bethe [1]. He found that, at first approximation, the normalized-to-area transmission through a circular hole perforating an infinitely thin perfect conductor plate is

$$T \approx \frac{64}{27\pi^2}\left(\frac{r}{\lambda}\right)^4 \tag{2.1}$$

where $\lambda$ is the wavelength of the incoming light, being $r$ the radius of the hole. It was a great surprise indeed, because most of the well established theories at that time gave a $(r/\lambda)^2$ dependence. Furthermore he found the pre-factor, not only that unexpected dependence. Bethe's theory shows that a subwavelength hole ($\lambda \gg r$) is a poor device for transmitting light through.

Therefore, it is not strange that the discovery of the phenomenon of extraordinary optical transmission (EOT) through subwavelength holes by Ebbesen et al. [2] has been one of most important findings in the field of Optics in the last years. The basic structure in which EOT phenomenon emerges is a two-dimensional periodic array of subwavelength holes (2DHA) perforated on an optically thick metallic film. This phenomenon is characterized by the appearance of a series of transmission peaks and dips in the transmission spectrum. It is commonly accepted EOT occurs when the normalized to area transmission is larger than unity. On the other hand, when the transmission per hole in an array is larger than for an isolated hole is called enhanced transmission. Here we will not differentiate between these two cases. From the beginning, it was realized that the spectral locations of those resonant features coincide with the corresponding ones of surface plasmon polaritons (SPPs) [3]. This link between EOT and SPPs has been corroborated by subsequent theoretical works

S. G. Rodrigo, *Optical Properties of Nanostructured Metallic Systems*,
Springer Theses, DOI: 10.1007/978-3-642-23085-1_2,

[4, 5] and now it is widely accepted that the excitation of those surface electromagnetic (EM) modes is at the origin of EOT.

The EOT mechanism has sparked considerable interest for its fundamental implications and also from the applied point of view, as many potential applications based on this phenomenon have been proposed [6]. EOT observed in symmetrically perforated thin metal films [2, 4, 7, 8], the squeezing of the optical near-field by plasmon coupling resulting in focusing light into very small volumes [9], and beaming of light via a single slit (or hole) in thin metal films surrounded by a grating like structure [10] are only a few of many interesting examples. A vast number of applications have been suggested and some are currently in use, e.g., wavelength tunable filters, subwavelength lithography, near-field microscopy, surface enhanced Raman spectroscopy, etc. Obviously, it is out of the scope of this chapter to review so wide field of research. We recommend for further reading Ref. [6, 11, 12], and references therein.

Throughout this chapter, we just summarize a part of the contributions to EOT done during the course of this thesis [13–16]. In these works our aim was trying to understand some important aspects of the EOT when the parameters defining the structure presenting EOT are varied. It what follows we will discuss how EOT depends on: the metal chosen, the shape of the holes and the film thickness. The study will focus on the optical response of 2DHAs drilled on metal films. Additionally, we will investigate a quite different system that also displays EOT. The chapter is organized as follows:

a. In Sect. 2.2, we present a theoretical study, based on the finite difference time domain (FDTD) method, of the optical response of circular hole arrays drilled in several metal films (Ag, Au, Cu, Al, Ni, Cr and W). Two series of structures are studied. In the first one, transmittance peaks are analyzed as all geometrical parameters defining the system are scaled, except the metal thickness which is kept constant, showing a good agreement with existing experimental data. In the second series, also the metal thickness is scaled. These is no available experimental data for this case, but its theoretical consideration allows a clear distinction in the behavior of different metals.
b. A theoretical study is developed on the optical transmission through square hole arrays drilled in optically thin films in Sect. 2.3, by means of the FDTD method. Nano-structures containing thin films are interesting because transmission may occur through both the holes and the metal layer. Moreover, the EM bounded modes supported by thin films are not the same that those supported by thick films.
c. It is known two mechanisms leading to enhanced transmission of light in 2DHAs: excitation of SPPs and localized resonances that are also present in single holes. In Sect. 2.4 we analyze theoretically how these two mechanisms evolve when the period of the array is varied. Along with the FDTD method this work was also done with the aim of the coupled mode method (CMM). This method was adapted to this problem by Dr. A. Mary at the Departamento de Física Teórica de la Materia Condensada—Universidad Autónoma de Madrid.

d. Finally, in Sect. 2.5, the spectral dependence of the extraordinary transmission through monolayers of close-packed silica or polystyrene microspheres on a quartz support, covered with different thin metal films (Ag, Au and Ni) is investigated. Measured spectra are compared with modeled transmission spectra using FDTD calculations. The optical response of this system shows remarkable differences as compared with the "classical" 2DHA configuration.

## 2.2 Influence of Material Properties on EOT Through Hole Arrays

Pioneering attempts to understanding EOT pointed out to SPP modes [2, 4, 17, 18] as responsible for the phenomenon. More generally, it has been shown that EOT-like behavior occurs whenever two surface modes are coupled between themselves and weakly coupled to a continuum [4], allowing a Fano-like description of the process [19]. Examples of this general mechanism are the cases of wave transmission aided by: Brewster-Zenneck waves in hole arrays drilled in Tungsten [20], guide cavity modes on slit arrays covered by a dielectric layer [21], surface electromagnetic waves in photonic crystals [22–24], surface sonic waves [25], and even the transmission of cold atoms through optically induced potential barriers [26].

Back to the case of 2DHAs, many studies have been devoted to study the dependence of EOT on the different parameters defining the system. As regards to geometrical parameters, it has been found that the hole shape can strongly influence both the polarization properties and the intensity of the transmission. This has been related to the presence of single-hole transmission resonances that couple to the SPPs [15, 27–31].

With respect to the material properties, it is known that some metals (notably Au and Ag) are best suited for EOT than others (Ni, Co,...) [2, 3]. However, a systematic comparative between different metals was lacking until the experiments performed by Przybilla et al. were reported [32]. These experiments analyzed EOT through 2DHA made of circular holes drilled in optically thick metal films, deposited on a glass substrate. The study considered different metals and analyzed the peak transmittance as a function of lattice parameter which, in turn, controlled the resonant wavelength. If the system were a perfect electric conductor (PEC) the transmission would not depend on lattice parameter, provided all length scales in the system are scaled in the same way. Therefore, deviations from this behavior reflects the effect of material properties. In the experiments [32] the hole radii were scaled with the lattice parameter but, due to practical limitations, the metal thickness was kept constant, which makes the analysis even more complex. Another possible complication is that finite size effects, surface quality and imperfections in hole shape in a real system could depend on the metal considered.

In this section we present a theoretical study of EOT in periodic hole arrays drilled in different metals. First we compare with the experimental results presented

in Ref. [32]. Additionally, we present a study in which *all* lengths are scaled with the lattice parameter. In both cases, comparison with the PEC case helps to understand the effect of material properties in the light transmission through 2DHA.

### 2.2.1 Theoretical Approach

Our calculations are performed with the FDTD method (See Sect. 1.2). Infinite periodic 2DHA are simulated by applying Bloch conditions at the boundaries of the unit cell and imposing "uniaxial perfect matched layers" at surfaces parallel to the metal film. In the FDTD method Maxwell's equations are discretized in both space and time. Therefore, convergence depends on both mesh size and temporal step. In order to properly calculate the influence of material properties, the rapidly decaying fields inside the metal should be accurately computed. This, together with the proper representation of circular holes in cartesian coordinates (which are the natural choice for square arrays in a film), impose very small mesh sizes. In this section we use mesh sizes ranging from 2 to 5 nm. The dielectric constant in cells at the metal-dielectric interface is taken as that of the medium with largest volume inside that particular cell.

For the calculation of the transmittance, the structures were excited by a gaussian wave-packet composed of normally incident plane-waves (with the electric field pointing along one of the axes of the square array) and all frequencies of interest (Sect. 1.2.2). Spectra were calculated after projection onto diffracted modes (Sect. 1.2.3). In the comparison with experimental data, only the zero order mode was considered in the post-processing, as experimental intensities were collected in a small solid angle centered around the normal direction. Additionally, in our study we will correlate transmittance features to the dispersion relation of modes supported by the corrugated slab. For this, the band structure is calculated exciting the system with a superposition of Bloch's waves with a well defined crystal momentum, and imposing Bloch's theorem at the boundaries (Sect. 1.2.3).

Metals require a special treatment in FDTD method because of the dielectric constant is local in frequency domain but non-local in the time-domain, as explained in Sect. 1.2.4. We have used the "piece linear recursive convolution method", which can efficiently treat dispersive media, provided their dielectric constant $\varepsilon(\omega)$ can be expressed as a sum of Drude and Lorentz terms:

$$\epsilon(\omega) = \epsilon_r - \sum_j \frac{\omega_{Pj}^2}{\omega(\omega + \imath\gamma_j)} - \sum_j \frac{\Delta\epsilon_j \Omega_j^2}{\omega^2 - \Omega_j^2 + \imath\omega\Gamma_j}. \tag{2.2}$$

We have considered the following materials: Ag, Au, Cu, Al, Ni, Cr, and W, taking the values for the parameters in the Drude-Lorentz form either from the literature (when available) [33, 34] or from fits to data in Palik's handbook [35, 36]. The fitting parameters used were given in Table 1.1, and the wavelength dependence of the dielectric constant obtained from them is depicted in Fig. 2.1 for reference. Also for

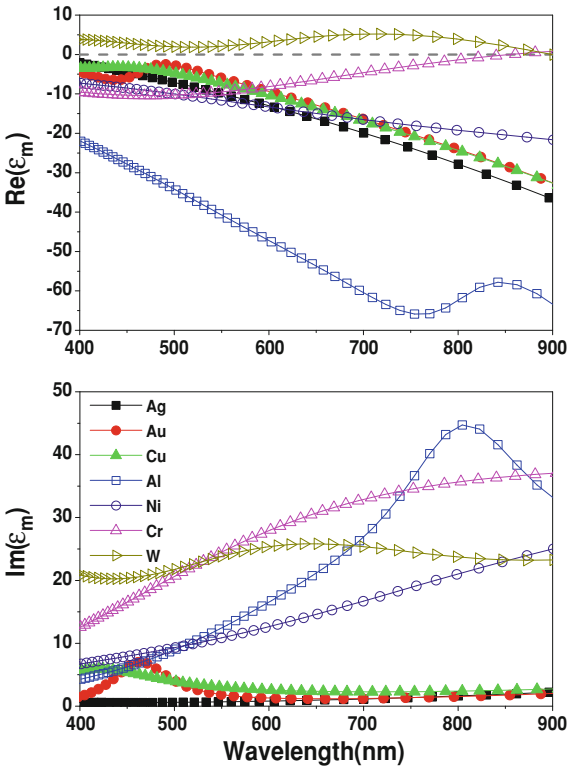


**Fig. 2.1** Dielectric constant for Ag, Au, Cu, Al, Ni, Cr and W, as a function of wavelength (obtained with Eq. 2.2 from data in Table 1.1)

future reference, Fig. 2.2 renders both the skin depth, $\delta = [Im(k_m)]^{-1}$ (with $k_m^2 = \varepsilon_m \omega^2/c^2$) and the SPP absorption length, $L_{\mathrm{SPP}} = [2Im(k_{\mathrm{SPP}})]^{-1}$, being $k_{\mathrm{SPP}} = (\omega/c)(\varepsilon_S \varepsilon_m/(\varepsilon_S + \varepsilon_m))^{1/2}$ the SPP longitudinal wavevector. Here $\varepsilon_m$ and $\varepsilon_S$ are the metal dielectric constant and the substrate dielectric constant, respectively. We stress here that the dielectric constants used in this study are taken directly from experimental data on bulk. No attempt has been made to improve the comparison between computed and experimental transmission spectra by incorporating additional fitting parameters.

## *2.2.2 EOT Peak Related to the Metal-Substrate Surface Plasmon*

### Peak Position

Figure 2.3 renders the FDTD results for the transmittance spectra of an array (lattice parameter $P = 400$ nm) of circular holes with diameter $d = P/1.75 \sim 230$ nm in different metal films. In all cases, the metal thickness is $w = 250$ nm, and the films

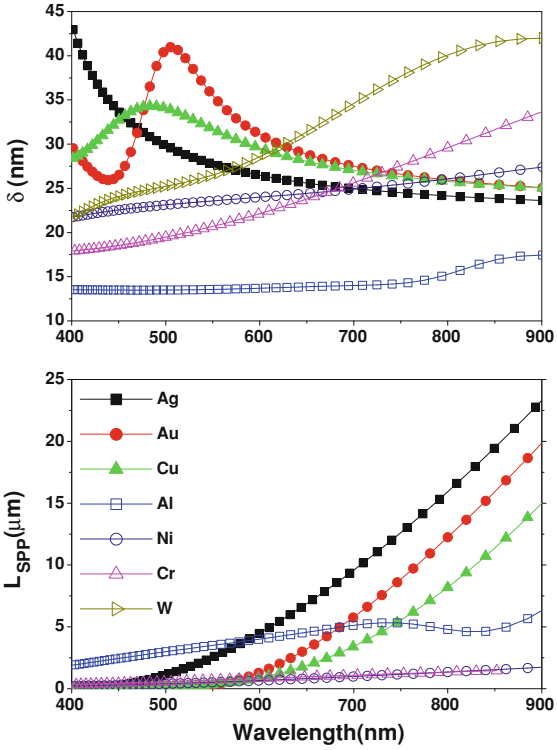


**Fig. 2.2** Spectral dependence for different metals of (**a**) skin depth for a plane wave impinging at normal incidence on the metal surface (**b**) absorption length for SPP on the metal-dielectric interface

are deposited on a substrate with dielectric constant $\varepsilon_S = 2.25$. The figure clearly shows the difference in transmittance spectra between different metals. We also include the calculation for W which, in the considered frequency range, is a dielectric, i.e., $Re(\varepsilon_W) > 0$. Notice that the heights of EOT peaks in W are even smaller than those of the "bad" metals (Ni and Cr). Notice also that W has a transmission maximum very close to the Rayleigh condition, $\lambda_R = \sqrt{\varepsilon_S} P$, wavelength at which the $(1, 0)$ diffraction order changes character from evanescent to radiative, while the corresponding one in the metallic case is red-shifted (by as much as $\approx$125 nm in the case of the "good" metals in the optical regime: Ag, Au, Cu). In the rest of this section, and following Ref. [32], EOT is characterized by the transmittance peak appearing close to $\lambda_R$. More precisely, in the metallic case, this peak is related to the spectral location of the SPP of the corrugated structure [4, 32, 37]. Here we will label this peak as $S_{1,0}$. Figure 2.4 shows the $S_{1,0}$ peak spectral position (defined as $\lambda_{1,0}$) as a function of the period, for the parameters considered in Ref. [32] ($w = 250$ nm; $d = P/1.75$). In addition, Fig. 2.4 also renders the light line in the substrate (continuous line) and the results obtained by considering the metal as a PEC, i.e. a metal with $\varepsilon = -\infty$, with the same nominal parameters (asterisk data points). Notice that a flat metal surface does not support EM modes, but a periodically corrugated one behaves as if it had a Drude-like dielectric response in which the effective plasma frequency depends only

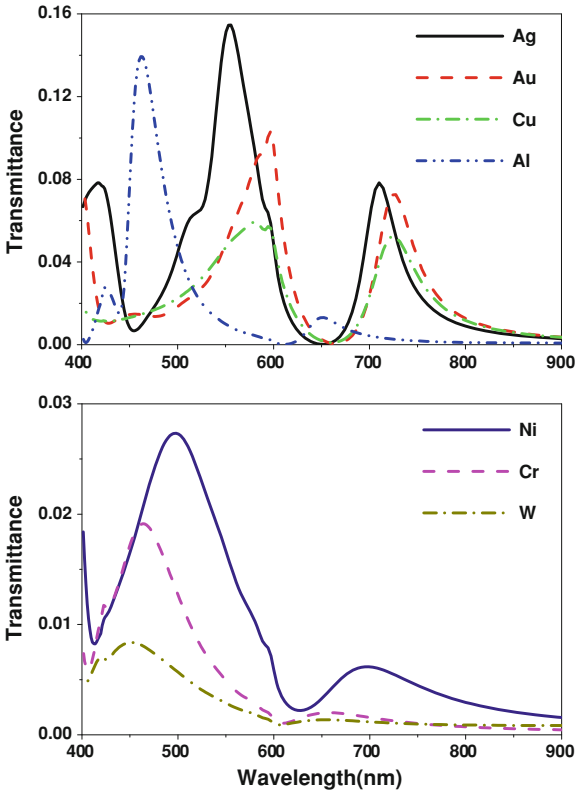


**Fig. 2.3** A representative case of computed transmission spectra, for the different metals considered. The geometrical parameters defining the array are: period $P = 400$ nm, metal thickness $w = 250$ nm and hole diameter $d = P/1.75$

on the geometrical parameters [38–40]. Thus, comparison with the PEC case allows to discern geometrically induced effects from the ones due to material properties. In any case, the agreement between these calculations and the experimental measurements (see Fig. 2.3 in Ref. [32]) is remarkable. The small differences could be attributed to variations in the actual dielectric constant from the bulk value, to finite size effects [41], and/or to irregularities on hole shape and size related to the small uncertainties from focused ion beam (FIB) lithography technique (which has an accuracy of the order of 10 nm). In our opinion, the agreement obtained validates FDTD calculations as a predictive tool in this kind of systems. These results also confirm that, in the experiments considered, the effect of possible inhomogeneities in hole shape and size was not relevant. Notice that the good agreement with the experimental data was obtained by using the bulk dielectric constant, despite the fact the dielectric properties at the surface could have been modified by the processing related to drilling of the holes.

In order to obtain further insight on the origin of EOT phenomena, Fig. 2.5 renders the dependence with period of $\lambda_{1,0}$ for the metals Ag and Al, and also for W. In this figure, we have also included the spectral location of the minimum which appears

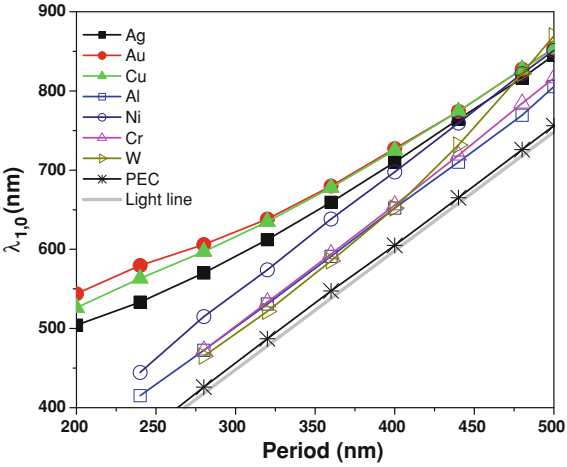


**Fig. 2.4** (1,0) substrate peak position, $\lambda_{1,0}$, as a function of the array period, both for the metals investigated and for a perfect electrical conductor. Hole radius is scaled with the period as $d = P/1.75$ but film thickness is kept constant at $w = 250$ nm

associated to the $S_{1,0}$ peak, slightly blue-shifted from the maximum. Results are presented for the case of constant film thickness, $w = 250$ nm. In the same figure we represent both $\lambda_R$ and the folded dispersion relation for the SPP of a *flat* metal-dielectric interface (given by the expression $(\omega/c)(\varepsilon_S\varepsilon_m/(\varepsilon_S + \varepsilon_m))^{1/2} = 2\pi/P$).

In the case of metals, the correspondence between transmittance minima and SPP of the flat surface (with no holes) is evident from the figure, with the maxima following the same trend at slightly longer wavelengths. In the case of the dielectric (W), both maximum and minimum have much smaller amplitudes with respect to the transmission background than in the case of metals (see Fig. 2.3), with the very weak minimum appearing at $\lambda_R$. Both maximum and minimum are related to the surface EM modes of the corrugated structure. More precisely, each surface EM mode has associated a maximum and minimum transmission, characterized by a resonant Fano-like function times a smooth function related to the coupling of the incident wave with the surface mode. At normal incidence, the incident wave can couple to SPPs in the periodically corrugated structure which originate from plane waves differing from $\vec{k}_{\parallel} = 0$ by a reciprocal lattice vector. This is confirmed by Fig. 2.6, which renders the folded light line, the folded SPP dispersion relation of the flat metal-vacuum interface, and the FDTD calculation for the band structure of surface EM modes of the corrugated surface.

### Transmission Intensity

Up to here we have concentrated on the dependence of the spectral position of transmission anomalies with the period of the array. The results for the peak intensities are presented in Fig. 2.7, which renders the maximum transmittance of the $S_{1,0}$ peak, $T_{1,0}$, as a function of its spectral position (i.e. for different periods) for several materials. In panel (a) all lengths defining the system are scaled with the period,

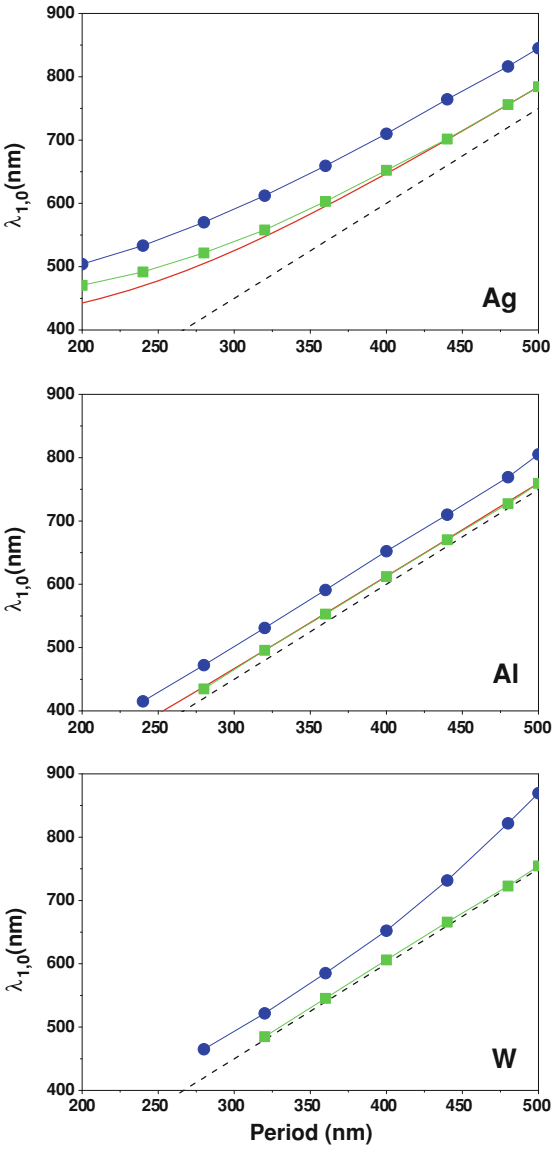


**Fig. 2.5** Dependence on period of signatures related to the (1,0) substrate peak: maximum (*circular symbols*) and minimum (*square symbols*). Hole radius is scaled with the period as $d = P/1.75$ but film thickness is kept constant at $w = 250$ nm. The *solid red line* represents the SPP dispersion relation for a flat metal-dielectric interface, while the *dashed black line* corresponds to the dielectric light line

except the metal thickness, which is kept constant at $w = 250$ nm (this is the case considered in Ref. [32]).

In panel (b) all lengths are scaled with the period. In this latter case, if the metal were a PEC, the peak transmittance would not depend on period (line with asterisks). A real metal presents two main differences with respect to a PEC, each of them having an opposite effect on the transmittance. On the one hand, real metals absorb energy,

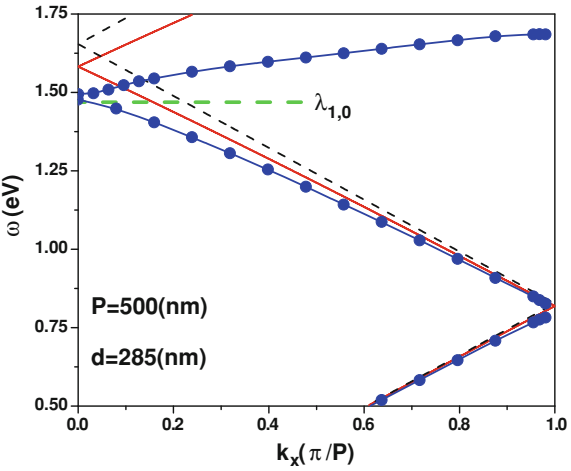


**Fig. 2.6** SPP dispersion relation in the $\Gamma - X$ direction of the first Brillouin zone, for the dielectric-silver interface. *Circular symbols* (*blue line*) show the FDTD band structure for a 2DHA with period $P = 500$ nm and metal thickness $w = 250$ nm. Flat surface SPP dispersion relation is depicted with a *solid red line*. *Dashed black line* represents the light line. The spectral position of the (1,0) transmission maximum, $\lambda_{1,0}$, is depicted by a *dashed horizontal green line*

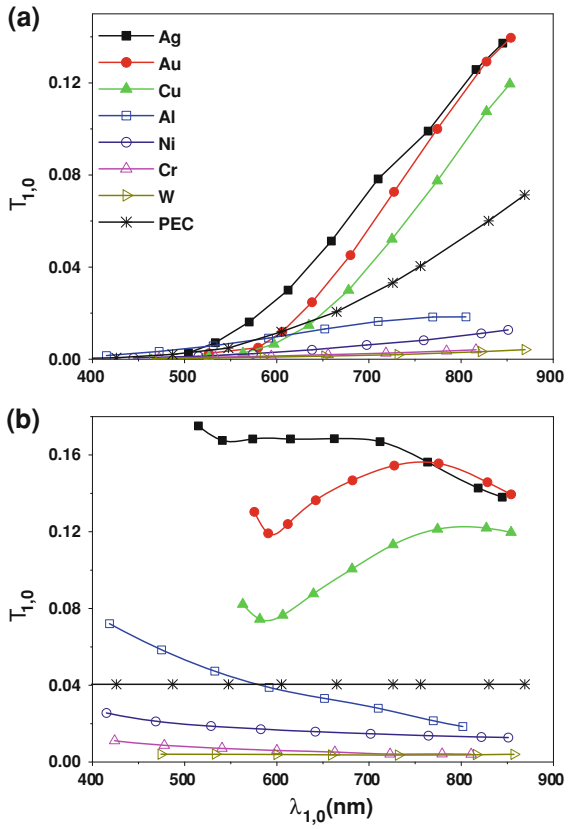


**Fig. 2.7** Peak transmittance intensity, $T_{1,0}$, as a function of the peak spectral position, $\lambda_{1,0}$ for different metals and lattice periods. In both panels, hole diameter is scaled with period as $d = P/1.75$. In (**a**) metal thickness is kept constant at $w = 250$ nm. In (**b**) $w$ is also scaled as $w = P/2.0$

which reduces the transmittance. This is more apparent in resonant processes, which require the EM field to stay for a longer time at the surface. As this resonance time is inversely proportional to the peak width, absorption has a larger influence on the narrowest transmittance peaks. On the other hand, the EM field penetrates in a real metal, effectively increasing the hole area accessible to the field and, therefore, increasing the transmittance. Several approximations can be envisaged in order to take into account the effective hole area. For instance, the hole can be considered as a finite portion of a waveguide. Effective areas can then be related to the propagation constants and the EM fields of different modes in the waveguide [42]. A simpler, phenomenological, approach is implemented by enlarging the hole radius by a factor (of order unity) times the skin depth [4]. This is a good approximation, provided the correction (skin depth) is much smaller than the hole radius. In any case, the effective hole area depends on the dielectric constant which, in turn, depends on wavelength. Therefore, from a electromagnetic point of view, even when all nominal lengths are scaled with the period, the "effective" surface percentage covered by holes does not remain constant. In what follows, we will show how the comparison with the PEC case allows to distinguish which of these two competing mechanisms (absorption and enlargement of the effective area) dominates for a particular circumstance. Let us start with the case of silver. The computed peak transmittance for silver is even larger than the corresponding one in a PEC *with the same nominal parameters*, as shown in Fig. 2.7. This suggest that, in this case, the "enlargement of effective area" mechanism is more important than absorption. In order to confirm this point, we have computed the transmittance peak intensities for 2DHA in PEC, but with the hole radius enlarged by the skin depth in Ag (computed at the wavelength at which the peak appears). We will refer to this as the "Corrected-PEC model". Figure 2.8 renders the results of these calculations, as well as the corresponding ones for 2DHA in Ag. Discontinuous lines represent the case in which all lengths in the system have been scaled with the period, except the metal thickness, which has been kept constant at $w = 250$ nm. The continuous lines render the case where also the metal thickness has been scaled with the period, as $w = P/2$. In all cases, the difference in transmission peak intensities between 2DHA in Ag and the enlarged holes in PEC is less than 30%. Notice that the Corrected-PEC model provide much more accurate results at large periods than at smaller ones, which can be associated to the increasing effect of absorption occurring at shorter periods and, correspondingly, smaller wavelengths. This is further corroborated by the fact that, at small periods, the Corrected-PEC model overestimates the peak transmittance.

This analysis helps understanding the results presented in Fig. 2.7b, and therefore the relative importance of the previously described mechanisms for different metals. At peak positions larger than $\lambda_{1,0} \approx 700$ nm, the dependence of $T_{1,0}$ on $\lambda_{1,0}$ for Au is similar to that of Ag, reflecting their similar skin-depths and absorption lengths. As $\lambda_{1,0}$ decreases, the difference in skin-depths in Au and Ag remains constant, but the ratio of their absorption lengths decreases. Correspondingly, due to absorption, $T_{1,0}$ in Au is smaller than that in Ag in this frequency regime. At the shorter $\lambda_{1,0}$ computed for Au this decreasing tendency is reversed, reflecting the increase in the skin-depth of Au (notice that the flattening out of the $\lambda_{1,0}$ versus period curve prevents exploring shorter

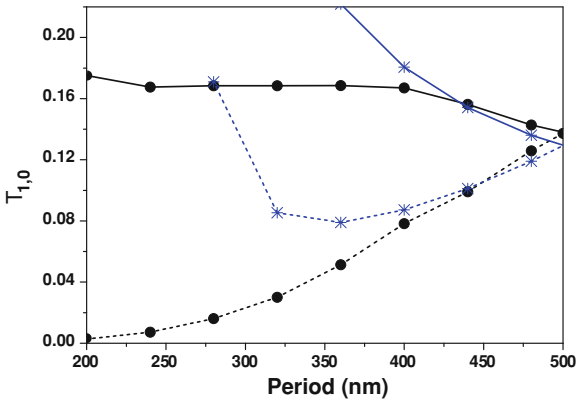


**Fig. 2.8** Peak transmittance, $T_{1,0}$, as a function of the lattice period for silver (*circular symbols*) and PEC (*asterisks*). *Solid line* represents the case of scaled thickness ($w = P/2.0$), while the *dashed line* is for constant $w = 250$ nm. In the PEC case, the hole radius was enlarged by one silver skin depth (Fig. 2.2), evaluated at the corresponding wavelength

values of $\lambda_{1,0}$, see Fig. 2.4. To summarize, optical transmissions through 2DHA in Ag and Au are similar: in both cases the resonant transmission is larger than in a PEC with the same nominal parameters, the effect being caused by field penetration inside the metal, which effectively enlarges the hole area. Absorption is not the main factor for these metals. On the other hand, 2DHA in Cu have transmittance peak characteristics similar to those in Ag or Au, but with smaller values, reflecting the smaller absorption lengths in Cu than in the other two noble metals analyzed.

A completely different behavior occurs for a 2DHA in Ni or Cr: in both cases, the peak transmittance is always much smaller than that in Ag (or in a PEC). This behavior occurs although the skin depth in these metals can even be larger than in Ag, and is due to the large absorption present in both Ni and Cr.

Hole arrays in Al have transmittance peak characteristics more similar to the PEC case, reflecting the fact that the skin depth in Al is, at optical frequencies, much smaller than those of the other metals. Even so, $T_{1,0}$ depends on $\lambda_{1,0}$ for 2DHA in Al: the skin depth in Al remains approximately constant with wavelength, implying an "effective area" correction which is relatively smaller at larger hole areas (i.e., larger periods and larger $\lambda_{1,0}$ in the case in which all *nominal* lengths are scaled). This explains why, in this case, $T_{1,0}$ decreases with $\lambda_{1,0}$ even if the absorption length slightly increases (see Fig. 2.2) Notice that this behavior of the absorption length in Al is also very different to that in noble metals, where the absorption length increases strongly with wavelength. As a consequence, the absorption length in Al is, at $\lambda \approx 750$ nm, smaller than that in noble metals. This, combined with the unusually small skin depth makes that $T_{1,0}$ in Al has values of the order of those of "bad metals" (Cr, Ni) at the higher end of the spectral window considered. Finally, a 2DHA perforated in W present a very different transmission spectrum. As previously stated, in the considered spectral range W is a lossy dielectric. Transmission resonances are aided by Zenneck waves [20, 43], which are more weakly bound than SPPs. The resonances are much weaker, with a much smaller "visibility": the minima are not very deep and the maxima are not as high as in the case of metals (see Fig. 2.9). Also,

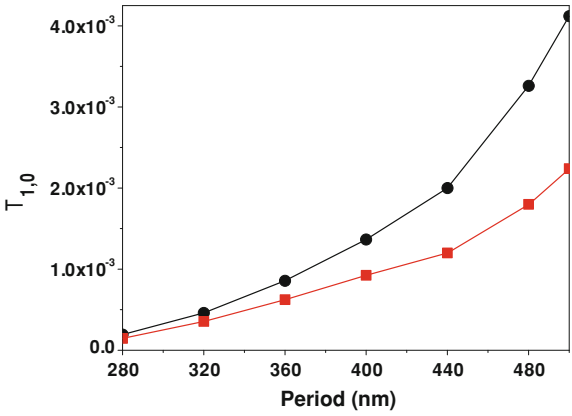


**Fig. 2.9** Dependence on period of features of the $S_{1,0}$ peak in W: Maximum (*circular symbols*) and minimum transmittance (*square symbols*). All lengths have been scaled as in Fig. 2.7a

as mentioned before, the spectral position of $T_{1,0}$ in W (appearing very close to $\lambda_R$) is different to that of the metallic case.

**Full-Width-at-Half-Maximum**

The previous analysis on the relative importance of the skin depth and absorption length on the transmittance through 2DHA, based on the peak intensities, is reinforced by the spectral dependence of the peak linewidth. Figure 2.10 renders $\Gamma_{1,0}$, defined as the the full width at half maximum (FWHM) of the $S_{1,0}$ transmittance peak, as a function of $\lambda_{1,0}$. The calculations were performed for the configuration where all lengths are scaled, except the metal thickness which is kept fixed at $w = 250$ nm. Agreement between experiment [32] and theory is quite good, although experimental peaks are wider due to finite size effects and/or sample imperfections. The behavior of $\Gamma_{1,0}$ for a 2DHA in Au, Ag and Cu is similar. In this case, and for the parameters considered, radiation is the main loss channel for the surface EM mode, absorption being a (non-negligible) correction. Absorption is responsible for both the difference in $\Gamma_{1,0}$ between different metals and the decrease of $\Gamma_{1,0}$ with $\lambda_{1,0}$ (following the increase of the absorption length with wavelength). In the cases of 2DHA in either Cr or Ni, $\Gamma_{1,0}$ is much larger than that for noble metals, as expected, given that absorption lengths are much smaller in the former cases. Again, the case of Al is quite different from that of other metals: it goes from presenting the narrowest resonant peaks at small $\lambda_{1,0}$ to having values of $\Gamma_{1,0}$ of the order of those of "bad metals" for the larger $\lambda_{1,0}$ considered.

## 2.3 EOT Through Hole Arrays in Optically Thin Metal Films

As we have stated in the last section, since the discovery of EOT [2], numerous works have explored different parameter configurations of 2DHAs [6]. In the now

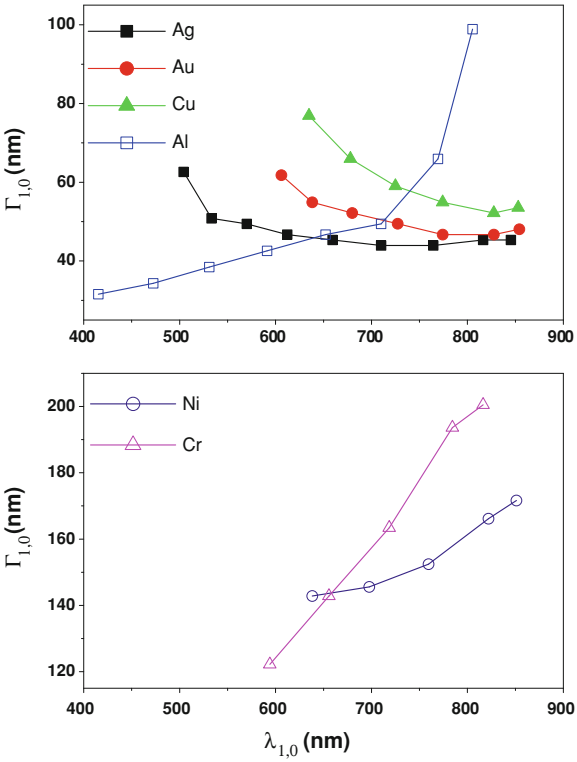


**Fig. 2.10** Full width at half maximum for the $S_{1,0}$ peak, $\Gamma_{1,0}$, for 2DHAs in different metals. All lengths have been scaled as in Fig. 2.7a., i.e. the metal thickness is kept constant at $w = 250$ nm)

"canonical" configuration [2] the metal film is opaque. In this case, the EOT process involves surface modes at each side of the film which couple through the holes [4]. On the other hand, continuous metal films (thin enough to be translucent) also present transmission resonances when periodically corrugated. In this configuration, resonant spectral features are related to SPPs of the thin film [44, 45], the so called Short Range SPPs (SRs) and Long Range SPPs (LRs) [46].

The transmission of electromagnetic radiation through 2DHA, for thicknesses of the metal film ranging from less than 1 to 2–3 skin depths has been studied in the THz regime [47, 48]. These works showed how the intensity of the EOT peak developed with metal thickness, its spectral position being mainly determined by the lattice parameter. In this section, we extend the study to the optical regime. We analyze the optical response of 2DHAs on metal thickness, $w$, going from optically thick films to films as thin as approximately one "skin depth" ($\sim 20$ nm).

To provide mechanical stability, actual thin films must lie on a substrate, which we take to be glass. We consider two different dielectric configurations: the asymmetric ($\varepsilon_I = \varepsilon_{II} = 1.0\,;\ \varepsilon_{III} = 2.25$) and the symmetric one ($\varepsilon_I = \varepsilon_{II} = \varepsilon_{III} = 2.25$), which can be experimentally obtained by using an index matching liquid. Throughout this section we consider square lattices of square holes; the period, $P$, is chosen to be

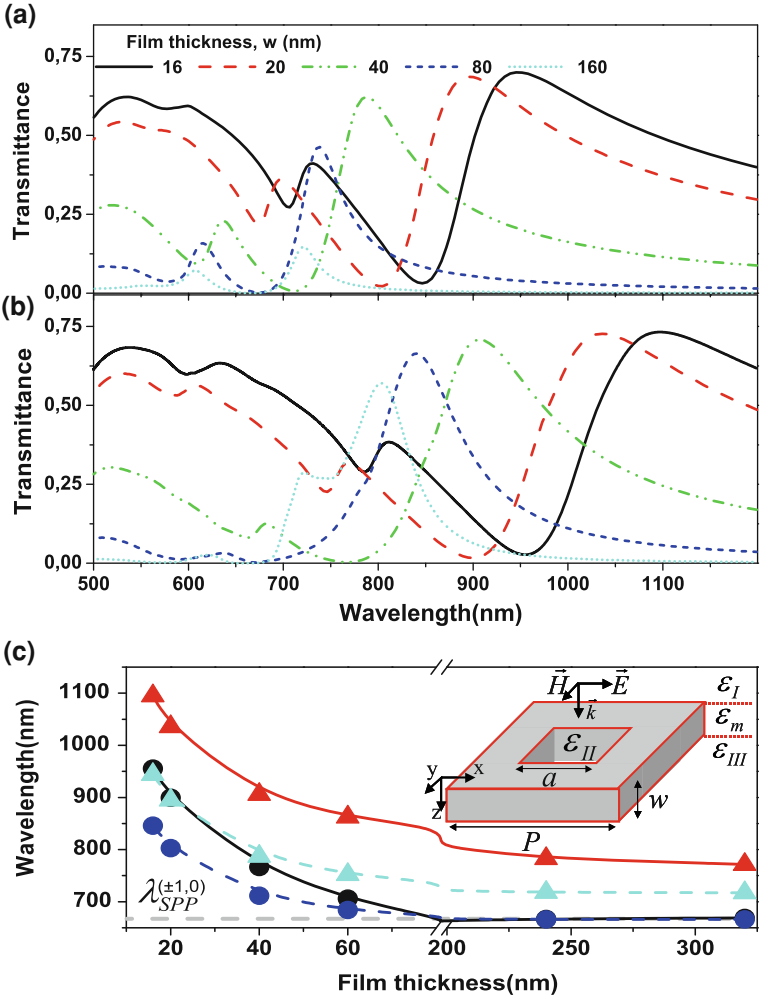


**Fig. 2.11** Zero-order transmittance through 2DHAs in gold, as a function of the film thickness ($P = 400$ nm, $a = 160$ nm) **a** $\varepsilon_I = \varepsilon_{II} = 1.0$; $\varepsilon_{III} = 2.25$ **b** $\varepsilon_I = \varepsilon_{II} = \varepsilon_{III} = 2.25$. The spectral position as a function of $w$ for both the EOT maximum (*triangular symbols*) an the EOT minimum (*circular symbols*) are shown in (**c**). *Dashed lines* summarize data obtained from (**a**), while *solid lines* are used for data taken from (**b**). The *horizontal dashed line* renders $\lambda_{\mathrm{SPP}}^{(\pm1,0)}$. From Ref. [14]

400 nm (in order to obtain EOT in the visible). The metal is gold (with a frequency dependent dielectric constant, $\varepsilon_m$ taken from Table 1.1). A schematic picture of the structure is shown as an inset in Fig. 2.11c.

Figure 2.11 renders the computed zero-order transmittance spectra through 2DHAs with different thicknesses, for both (a) asymmetric and (b) symmetric configurations.

Calculations have been conducted with the FDTD method. For optically thick films, we observe the "canonical" EOT resonant features appearing at wavelengths slightly red-shifted from the Rayleigh wavelength ($\lambda_R = \sqrt{\varepsilon_{III}}\, P = 600$ nm). As the film thickness is reduced, both maximum and minimum transmittance red-shifts by even hundreds of nanometers, while keeping high peak visibility.

In order to understand these spectral shifts, we analyze the EM modes bounded to the metal film. A flat unperforated optically thick metal layer supports a SPP on each surface. When the film thickness is reduced, these two modes interact, and are substantially coupled whenever the film thickness is smaller than 2–3 skin-depths. In this case, the dispersion relations of film modes can greatly differ from that of the SPP, while in the THz regime they remain close to the light line. We denote by $\vec{q}_{\text{mode}}(\lambda)$ the in-plane wavevector of these film modes (where the label "mode" can be either SPP, LR or SR) as a function of the wavelength $\lambda$. These film modes couple to external radiation and may lead to transmission resonances which, for small corrugations, are therefore expected to occur close to wavelengths satisfying:

$$\left(k_x^{in} + \frac{2\pi n}{P}\right)^2 + \left(k_y^{in} + \frac{2\pi m}{P}\right)^2 = q_{\text{mode}}^2(\lambda) \tag{2.3}$$

Here, the in-plane component of the incident wavevector is $\vec{k}^{in} = (k_x^{in}, k_y^{in})$, and $n$ and $m$ are integers. From now on, we denote by $\lambda_{\text{mode}}^{(n,m)}$ a wavelength that holds Eq. 2.3 at normal incidence ($\vec{k}^{in} = 0$), for some given values of $n$ and $m$. Figure 2.11c shows the spectral positions of both minimum and maximum of the EOT peak appearing at largest wavelengths. We find that when the film is thick enough the EOT minimum very approximately coincides with $\lambda_{\text{SPP}}^{(\pm 1,0)}$ [49]. In contrast, both maximum and minimum red-shift as film thickness reaches the "optically thin" regime.

To analyze whether the EOT phenomenon through optically thin 2DHAs has its origin in the excitation of an EM mode bounded to the film, we focus on the symmetric configuration with $w = 20$ nm. Figure 2.12a shows the transmission spectra for 2DHAs with different hole sizes. Vertical dashed lines mark different SR diffracted orders together with $\lambda_{\text{LR}}^{(\pm 1,0)}$. The EOT spectral positions of both maximum and minimum wavelength approach $\lambda_{\text{SR}}^{(\pm 1,0)}$ as the hole size decreases. At the same time, the EOT peak visibility is progressively reduced as the hole size decreases (the dashed line shows the result for the uniform film). Additionally, there are several small dips in the transmission spectra, which will be discussed later.

In order to assign even more conclusively EOT features to EM modes of the perforated film, we have calculated the band structure of surface modes in the holey film. The result is depicted in Fig. 2.12b (circular symbols), for a 2DHA with $a = 60$ nm. The dispersion relations for the bounded modes of a flat film (folded into the first Brillouin's zone), are represented with continuous lines. As usual, due to the presence of holes, the modes are coupled at the Brillouin's zone edges leading to band-gaps. In the wavelength window shown here, only the mode at the high-$\lambda$ edge (labeled as $\widetilde{\lambda}_{\text{SR}}$) is related to an EOT peak at normal incidence, due to the structure symmetry [50, 51]. The dependence with hole size of $\widetilde{\lambda}_{\text{SR}}$, together with that of the spectral posi-

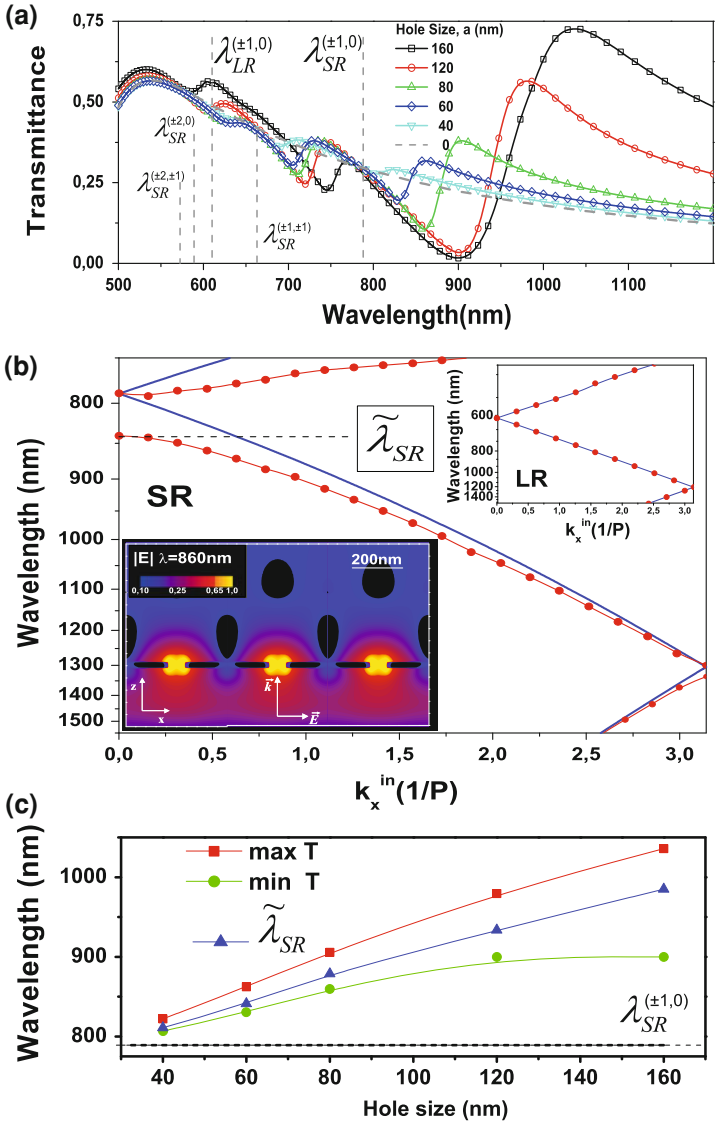


**Fig. 2.12** For a holey thin film with $w = 20$ nm ($P = 400$ nm and $\varepsilon_I = \varepsilon_{II} = \varepsilon_{III} = 2.25$), **a** shows transmittance versus wavelength for different hole sizes. Vertical dashed lines display several values of $\lambda_{LR}^{(n,m)}$ and $\lambda_{SR}^{(n,m)}$ (see text) at $k^{\vec{i}n} = 0$. **b** 2DHA dispersion relations along the x direction for $a = 60$ nm (*Circular symbols*). *Solid lines* represent the folded dispersion relations of LR and SR modes for the unperforated film. The *inset* in (**b**) shows a $|E|$ field map in the x-z plane ($y = P/2$) at the EOT wavelength. **c** EOT maxima (*square symbols*), minima (*circular symbols*) and $\widetilde{\lambda}_{SR}$ (*triangular symbols*) as a function of the hole size. From Ref. [14]

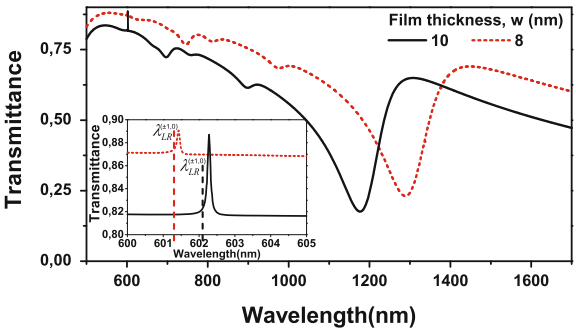


**Fig. 2.13** Transmission spectra for two different film widths obtained with the approximate analytical method: $w = 10$ nm and $w = 8$ nm ($a = 160$ nm). *Inset* zoom close to the LR wavelengths (Corresponding $\lambda_{LR}^{(\pm 1,0)}$ wavelengths are represented by *vertical dashed lines*). From Ref. [14]

tions of both maximum and minimum transmittance is displayed in Fig. 2.12c. For each hole size $\widetilde{\lambda}_{SR}$ lies between the spectral positions of the transmission maximum and minimum. Nevertheless, as the hole size shrinks to zero, the minimum of transmittance tends to $\widetilde{\lambda}_{SR}$. The inset of Fig. 2.12b renders a $|E|$ field map at the EOT peak wavelength, showing that the field enhancement around the holes [17, 37] is also present in optically thin films.

Interestingly, LRs do not noticeably contribute to transmission in the FDTD calculations (Fig. 2.12a). Notice that, due to the antisymmetric charge distribution of the LR, its field is almost negligible inside metal and it is less bounded to the surface than a SR mode. Therefore, the LR is both less absorbed and worse coupled to radiation than the SR. In short, the LR field is perturbed very weakly by the holes, so the coupling with the incident light diminishes. A consequence of this, is that the LR band structure for the drilled film virtually coincides with the unperforated one (Inset Fig. 2.12b). This weak coupling to radiation modes implies long times of the EM field standing at the surface. This suggest that the LR resonance could have been missed given the finite simulation time available. To be sure that LRs are not related to the shallow transmission dips, we have developed an approximate method for solving Maxwell's equations. In this method, the field is represented as a Fourier-Floquet series in the x-y plane and a power series in the coordinate perpendicular to the layer, $z$ [51]. This approach works only for extremely thin metal films (thinner than what is experimentally achievable in a continuous film nowadays), so it has mainly academic value. Nevertheless, it is useful for understanding the underlying physics. Figure 2.13 renders transmission spectra calculated with the approximate method for a 8 nm and 10 nm thin films. The zoom in wavelengths close to $\lambda_{LR}^{(\pm 1,0)}$ (inset to Fig. 2.13) reveals that extremely narrow peaks can be associated to LR modes. Anyway, spectral resolution within the FDTD method does not allow LR peaks to be resolved. The detection of this transmittance peaks due to LR plasmons would be even more difficult from the experimental point of view due to the finite size of the samples. In any case, this analysis shows that the small dips found with the FDTD method at short wavelengths are exclusively related to higher SR diffracted orders.

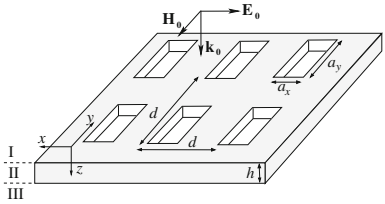


**Fig. 2.14** Schematic picture of a square array of rectangular holes of side $a_x$ and $a_y$ perforated on a free-standing silver film of thickness $h$. Parameter $d$ defines the period of the array. The apertures are illuminated by a p-polarized plane wave at normal incidence

## 2.4 The Role of Hole Shape on EOT Through Arrays of Rectangular Holes

Several works shown that the shape of the subwavelength aperture also has a great importance in the transmission spectra [27–29, 52, 53]. These studies demonstrated that elliptical or rectangular holes dramatically influence not only the resonant wavelength but also the polarization and the final transmittance. On the other hand, several experimental and theoretical works have shown that even a single rectangular hole exhibits a localized transmission resonance emerging at around the cutoff wavelength, $\lambda_c$, of the hole waveguide [30, 31, 42, 54]. This resonance can be understood as a Fabry-Perot resonance in which the propagation constant inside the hole is zero.

The aim of this section is to analyze in detail the interplay between these two types of transmission resonances (SPP and cut-off resonance) that are operating in a 2D array of rectangular holes. Figure 2.14 shows schematically the system under study: an infinite array of rectangular apertures of sides $a_x$ and $a_y$ perforated on a free-standing silver film of thickness $h$. The structure is illuminated by a p-polarized plane wave at normal incidence (i.e. incoming electric field is pointing along the short edge of the holes). In our calculations, we use the same geometrical parameters as those of the experiments carried out in Ref. [29]: $a_x = 200\,\text{nm}$, $a_y = 260$ nm and $h = 400$ nm. The period of the array, $d$, will be varied between 500 and 900 nm.

Figure 2.15b shows the normalized-to-area transmittance spectra corresponding to the geometrical parameters of Ref. [29], calculated with the couple mode method (CMM) (Sect. 1.3). To treat the metal properly, surface-impedance boundary conditions (SIBCs) are imposed on the metallic boundaries, except on the vertical walls of the holes which are treated as perfect conductor surfaces. To consider only the fundamental TE eigenmode ($TE_{01}$) in the modal expansion within the holes gives accurate results for the transmittance spectrum. As it was stated in Sect. 1.3, in order to improve the accuracy of the method realistic values for the propagation constant of the fundamental mode, $q_z$, are incorporated into the formalism by using the effective index method [55]. Note that the electric field of the $TE_{01}$ mode points along the $x$-direction, i.e., it is parallel to the short side of holes ($a_x$) and perpendicular to $a_y$. The properties of the two parallel real metal plates TM mode are the starting point

of the method. From its characteristic equation, it is obtained an effective dielectric constant ($\varepsilon_d$) as the ratio between the propagation constant of that mode and the vacuum one. This procedure follows to match the boundary conditions of the electric field across the long sides ($a_y$), for this reason the metal surfaces are separated by a distance $a_x$. Next, the effective index method takes into account the penetration of the electric field at the short axis by assuming the propagation constant of the TE mode (in the same system), but being in this case $a_y$ the distance between surface faces. Finally, the value of $q_z$ is obtained after solving the characteristic equation of such mode where the dielectric constant of the region between surfaces is set to $\varepsilon_d$. Note that by analyzing the location in which $q_z$ changes from being a real quantity to a purely imaginary magnitude, we can calculate $\lambda_c$ within this approach. For the particular set of geometrical parameters of the holes forming the 2D array here chosen, $\lambda_c = 695$ nm. Different curves correspond to different periods of the 2D square array (ranging from $d = 500$ to $d = 900$ nm). To compare them with the FDTD method results (Sect. 1.2), Fig. 2.15a depicts the corresponding transmission spectra obtained. It is clear that CMM is able to capture accurately the main features observed in the FDTD spectra. The locations and linewidths of the several peaks are well reproduced within the CMM approach. The heights of the transmission peaks are higher in CMM, mainly due to the fact that absorption within the vertical walls of the holes is neglected. It is also important to note that the theoretical results of panel (b) are in very good agreement with the experimental data [29].

Now we concentrate on analyzing the physical origin of the different transmission peaks appearing in Fig. 2.15b by just studying this simple formula for transmission (See Sect. 1.3):

$$T = \frac{|I_o|^2}{4\sqrt{\varepsilon}} \frac{G_i}{(G_i)^2 + \left(\frac{|G-\Sigma|^2-|G_v|^2}{2|G_v|}\right)^2} \tag{2.4}$$

For rectangular holes and within the SIBC approximation the different terms in Eq. 2.4 are:

The term $I_0$ measures the overlap between the incident plane wave and the 0-mode inside the hole:

$$I_0 = \frac{\imath\, 4\sqrt{2}}{\pi(1+Z_s)} \sqrt{\frac{a_x a_y}{d_x d_y}} \tag{2.5}$$

The term $G_v$ controls the coupling between the input and output sides of the holes:

$$G_v = \frac{2\, i\, Y_0\, e^{iq_z h}}{e^{2iq_z h}(1+Z_s Y_0)^2 - (1-Z_s Y_0)^2} \tag{2.6}$$

The expression for the *self-energy* $\Sigma$ is given by:

$$\Sigma = i\, Y_0 \frac{e^{2iq_z h}(1+Z_s Y_0) + (1-Z_s Y_0)}{e^{2iq_z h}(1+Z_s Y_0)^2 - (1-Z_s Y_0)^2} \tag{2.7}$$

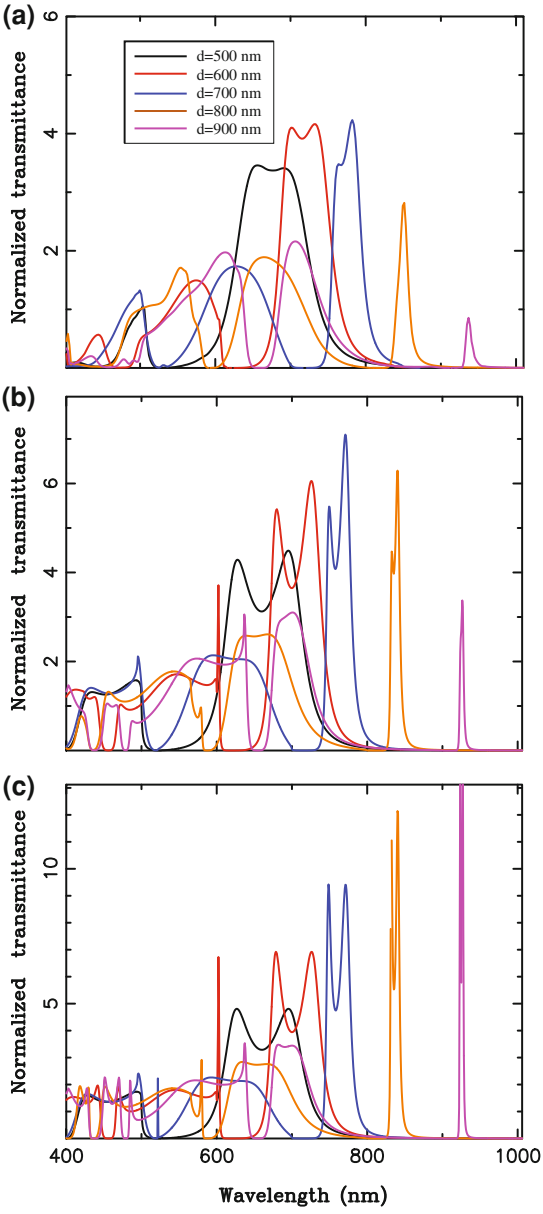


**Fig. 2.15**
**a** Normalized-to-area transmittances calculated with the FDTD method for different values of the lattice period $d$. **b** and **c** show the normalized-to-area transmittances calculated with the CMM. In (**b**), the dielectric function is that of silver whereas in (**c**) absorption of silver is neglected ($Im\,\varepsilon(\lambda) = 0$)

Finally, the EM-coupling between the holes forming the 2D array is mediated by the term $G$, which can be expressed as:

$$G = \frac{i\, a_x\, a_y}{2\, d_x\, d_y} \sum_{l=-\infty}^{l=+\infty} \sum_{m=-\infty}^{+\infty} \frac{k_0\,(k_0 + Z_s k_z) - k_m^2}{(k_z + Z_s k_0)\,(k_0 + Z_s k_z)} \times \operatorname{sinc}^2\left(\frac{k_l\, a_x}{2}\right) \left[\operatorname{sinc}\left(\frac{k_m a_y + \pi}{2}\right) + \operatorname{sinc}\left(\frac{k_m a_y - \pi}{2}\right)\right]^2 \tag{2.8}$$

with $k_l = \frac{2\pi}{d_x} l$, $k_m = \frac{2\pi}{d_y} m$, $k_p = \sqrt{k_l^2 + k_m^2}$ and $k_z = \sqrt{k_0^2 - k_p^2}$.

Here $Z_s = 1/\sqrt{\varepsilon_m}$ ( being $\varepsilon_m$ the dielectric constant of the metal), and $\varepsilon$ the dielectric constant of the surrounding media (in this case vacuum). On the other hand, $Y_0 = q_z/k_0$ corresponds to the admittance of the fundamental mode with $k_0 = 2\pi/\lambda$.

It can be demonstrated from Eq. 2.4 that transmission maxima and minima coincide with solutions of $|G - \Sigma| = |G_v|$, for 2DHAs at $\lambda > \sqrt{\varepsilon}\, d$. In other words, as in a typical resonant phenomenon the transmittance is governed by the behavior of the denominator. In Fig. 2.16 we show the dependence of both $|G - \Sigma|$ and $|G_v|$ versus wavelength for two limiting values of $d$, $d = 500$ nm and $d = 800$ nm (notice that $G_v$ does not depend on $d$). Interestingly, the spectral locations of the transmission peaks in Fig. 2.15b are marked by the cuts between $|G - \Sigma|$ and $|G_v|$. It is worth comparing the behavior of $|G - \Sigma|$ for the periodic arrays with $d = 500$, 800 nm with the corresponding $|G - \Sigma|$ for a single rectangular hole (dashed line in Fig. 2.16). The transmittance through a single rectangular hole is also governed by Eq. 2.4 but with a different $G$-term (the sum over diffractive modes in Eq. 2.8 is replaced by an integral over the continuous spectrum of plane waves). For $d = 500$ nm, $|G - \Sigma|$ (full black line) at the wavelength region of interest (near $\lambda = 700$ nm) is close to the single hole counterpart. It is expected then that the nature of the transmission resonances will be similar for a 2D array and for an isolated rectangular hole. However, there is a difference between the single hole case and the 2D array for this value of $d$. Whereas in the 2D array, $|G - \Sigma| = |G_v|$ at two different wavelengths (leading to two transmission peaks), for the single hole there is only one transmission peak appearing at a wavelength in which the difference between $|G - \Sigma|$ and $|G_v|$ is minimal. The reason of this distinct behavior stems from the Fabry-Perot nature of this transmission resonance. In a Fabry–Perot cavity, the spectral locations of the transmission resonances strongly depend on the reflectivity at the edges of the cavity. Our results indicate that the presence of a $2D$ array modifies the reflectivity of the metallic interface when compared to the single hole case, leading to the appearance of two transmission peaks. For $d = 800$ nm (blue line), $|G - \Sigma|$ present additional features located at $\lambda \approx 600$ nm and $\lambda \approx 800$ nm. These correspond to zeroes of the denominator of $G$ (see Eq. 2.8), appearing at the condition $k_z + Z_s k_0 = 0$. This condition is nothing else than the equation for the excitation of a SPP on a non-corrugated (no holes) surface of a metal film within the SIBC approach. Note that the cuts between $|G - \Sigma|$ and $|G_v|$ appears at wavelengths slightly larger than this condition. Therefore, the character of the two transmission peaks for $d = 800$ nm emerging at $\lambda \approx 830$ nm will be quite similar to a SPP. The two transmission peaks are associated with the symmetric and the anti-symmetric combinations of the two SPPs

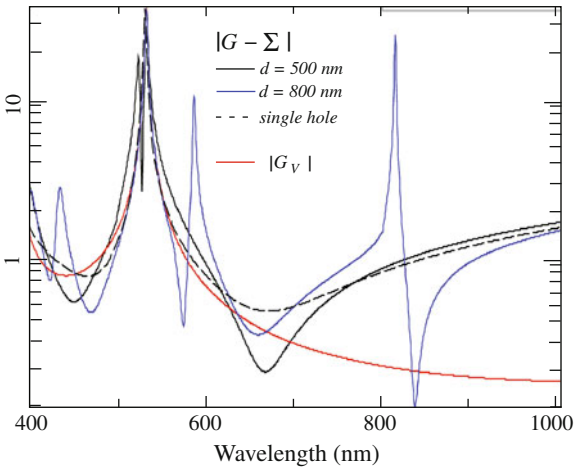


**Fig. 2.16** Absolute values of $|G - \Sigma|$ and $|G_v|$ terms (in logarithmic scale) for two different lattice constants of the hole array ($d = 500$ nm and $d = 800$ nm) and also for a single hole

at the two surfaces which are evanescently coupled through the holes, as explained in Ref. [4].

As a general conclusion about the nature of the transmission resonances appearing in 2D arrays, we could state that the two mechanisms leading to EOT (localized resonance and SPP-based) cannot be simply separated as done in previous studies [54] [see comment by Cheng-ping Huang and Yong-yuan Zhu, arXiv:0706.0250v1 (unpublished)] and [56]. Even for the shortest and the longest period considered here, the transmission resonances benefit from both mechanisms. Therefore, these transmission resonances have a hybrid character. Hybrid resonances have already been observed and studied previously in lamellar [57, 58] and bottle-shaped gratings [59]

The physical picture described above is reinforced when looking at the evolution of the electric field patterns associated with the resonant process as a function of $d$. In Fig. 2.17 we plot the E-field amplitude at resonance (normalized to that of the incident plane wave) evaluated at the $z = 0^-$ interface. Four periods are considered here: $d = 600, 700, 800$ and $900$ nm. The electric field amplitude for $d = 600$ nm is mainly concentrated over the holes as corresponds to the excitation of a localized resonance (cut-off resonance) inside the holes. As $d$ is increased, the character of the resonance changes gradually. For $d = 800, 900$ nm, the E-field intensity maxima are along the ridges of the holes as corresponds to a SPP wave propagating in the $x$-direction. For $d = 700$ nm, there is a mixing between the two mechanisms as fingerprints of the SPP wave begins to emerge at the edges of the holes. The near field distribution exhibits an intermediate character between the two limiting behaviors (SPP and cut-off resonances).

Finally, we would like to address the question of why there is a kind of optimum value for $d$ when looking at the evolution of the transmission peaks with the period of the array (see Fig. 2.15a,b). In our calculations this optimum $d$ is around 650–700 nm, close to the cut-off wavelength, 695 nm. Naively, this could imply that the optimum

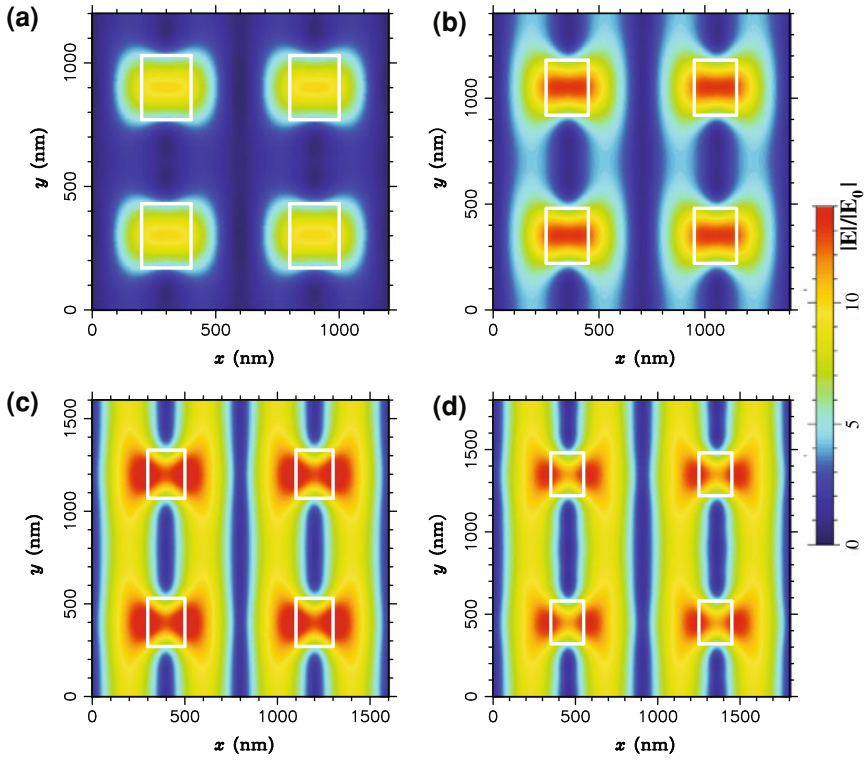


**Fig. 2.17** Electric field amplitude calculated at the resonant wavelength and evaluated at the $z = 0^-$ plane for **a** $d = 600$ nm, **b** $d = 700$ nm, **c** $d = 800$ nm and **d** $d = 900$ nm. The white lines mark the positions of the holes. The E-field magnitude is normalized to the incident one

$d$ appears when the resonant wavelengths of the two mechanisms (SPP and cut-off resonance) coincide. However, panel (c) of Fig. 2.15 demonstrates that the explanation is more complex. If the absorption in the metal is neglected, the heights of the transmission peaks grow with $d$ like $d^2$, as it would correspond to a perfect transmission (100%) per unit cell [60]. Therefore, EOT associated with SPP excitation is only limited by absorption. As explained above, absorption along the walls of the holes is not taken into account in the approximated model. However, we have checked that for all $d$ analyzed in this study, E-field intensity maxima are located at the horizontal metallic surfaces, where SIBCs are imposed within the modeling. Therefore, considering only absorption on top and bottom surfaces of the metallic film is a reasonable approximation when analyzing the evolution of the heights of the transmission peaks as a function of $d$.

Within this approach, it is worth defining two different lifetimes operating during the transmission process. By looking at the linewidth of the transmission peaks with no absorption (Fig. 2.15c), we can extract the lifetime associated with the resonant process, $\tau_{res}$. This quantity is related with the radiation losses as a result of the

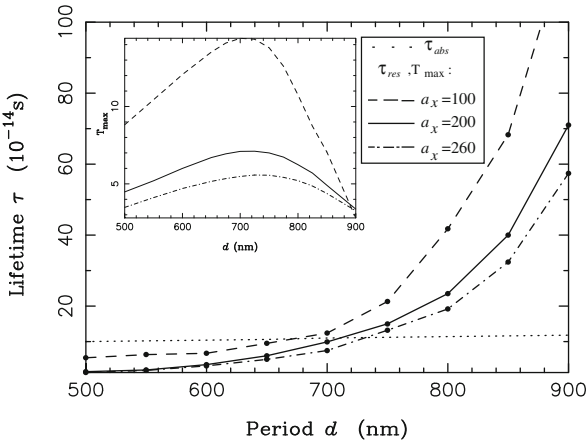


**Fig. 2.18** Absorption lifetime $\tau_{abs}$ (*dotted line*) and lifetime of the resonant process $\tau_{res}$ versus period of the hole array for $a_x =$ 100 nm (*dashed line*), $a_x = 200$ nm (*solid line*) and $a_x = 260$ nm (*dot-dashed line*). *Inset* Transmittance calculated at resonance versus $d$

coupling of holes to radiation. It is depicted in Fig. 2.18 as a function of the period of the array for three values of $a_x$ (200, 100 and 260 nm). As expected, when $d$ is increased, resonant lifetime grows rapidly. On the other hand, absorption introduces another time into the problem. From the knowledge of $\varepsilon(\lambda)$, we can estimate the time taken for a photon to get absorbed, $\tau_{abs}$. This lifetime is almost independent on $\lambda$, as shown in Fig. 2.18 (dotted line). It is expected that optimum $d$ would appear where $\tau_{res}(d) \approx \tau_{abs}(d)$. The line of reasoning leading to this naive rule is the following. When $\tau_{res}(d)$ is much smaller than $\tau_{abs}(d)$, photons are mainly transmitted and they are not absorbed by the metal. Absorption plays a minor role in the transmission process and the normalized-to-area transmittance at resonance increases when $d$ is increased, as seen in Fig. 2.15c. In the other limit ($\tau_{abs}(d)$ being much smaller than $\tau_{res}(d)$), photons are absorbed by the system before the resonance is built up. As $\tau_{res}(d)$ grows quadratically with $d$, a decrease of the transmittance at resonance versus $d$ is expected to occur in this limit. When interpolating between these two limits, it is clear that the curve displaying the transmittance at resonance versus $d$ should present a maximum for an *optimum* value of $d$. As $\tau_{res}(d)$ evolves very rapidly with $d$ whereas $\tau_{abs}(d)$ is almost independent on $d$, optimum $d$ should appear close to the condition $\tau_{abs}(d) = \tau_{res}(d)$. Figure 2.18 demonstrates that this last condition marks the location of the optimum $d$ for the three different values of $a_x$ analyzed. Therefore, we can safely conclude that the physical origin of the optimum $d$ observed in calculations stems from the absorption present in the metallic film.

Note that in the experiments [29], the finite size of the hole array introduces a third lifetime associated with the spatial extension of the array, $\tau_{size}$ [41]. As the absorption in the metal, it also acts as a limiting factor in the final transmittance. If the number of holes is large enough, $\tau_{size}$ is greater than $\tau_{abs}$ and then the limiting factor would be the absorption by the metal, as in the case of an infinite array. However, if the array is very small, $\tau_{size}$ would be smaller than $\tau_{abs}$ and finite size effects would control the optimum $d$. Then the cut between $\tau_{res}(d)$ and $\tau_{size}$ would mark the location of optimum $d$. If this is the case ($\tau_{size} < \tau_{abs}$), then the cut would appear at a shorter $d$.

This seems to be the case in the experiments reported in Ref. [29] as the experimental optimum $d$ is of the order of 600 nm, instead of a value close to 700 nm obtained from our calculations for an infinite array of holes (see Fig. 2.18).

## 2.5 EOT Through Metal-Coated Monolayers of Microspheres

Several papers on EOT involve experiments and simulations of metal films and gratings of rather simple geometry [2, 4, 8, 28, 61–66]. One drawback, considering applications, with these structures is that they are usually produced using a material removal focused ion beam and/or complex lithographic methods. In this section we analyze a quite different structure, namely, slabs of self-assambled arrays of dielectric microspheres covered with thin metallic layers. As we will see, these kind of systems present many similarities in their transmission properties with those in perforated metal films, with the advantage of being easily deposited over relatively large areas. Moreover, the following metal deposition can be done by standard techniques.

Monolayers of close-packed arrays of microspheres behave like two dimensional photonic crystal slabs (PCS) with photonic modes that may couple to the incident light. It has been shown that the strength of coupling and the position of the observed transmission dips could easily be altered by deposition of, e.g., amorphous Si onto the microsphere arrays [67, 68]. If the microsphere array is instead covered with a thin metal film, EOT through the slab has been observed [69]. Different mechanisms could be responsible for the EOT-like transmission features: Mie resonances of the spheres, transmission through the empty spaces left by the spheres after covering them with the metal,... [69]. In order to clarify the actual origin of the resonances observed, in this section we analyze a set of experimental results carried out in the group led by Prof. D. Bäuerle, from the Institute of Applied Physics Johannes-Kepler-Universitat in Linz (Austria). For this, we use the FDTD method discussed in Sect. 1.2. The good agreement between measured and modeled spectra allows further in-depth interpretation of the origin of the different features observed in the measured transmission spectra, highlighting the relevance of waveguide modes in the microsphere array on the EOT properties.

### *2.5.1 Methods*

#### Experiment

Microspheres of different materials have been utilized in various fields of research in the past few years. Examples of applications are micro-resonators with high quality factors [71], in mask lithography [70], and also as lens arrays for different types of laser-induced micro- and nano-patterning of material surfaces. In the case of laser-induced applications, close-packed 2D-lattices of usually transparent microspheres

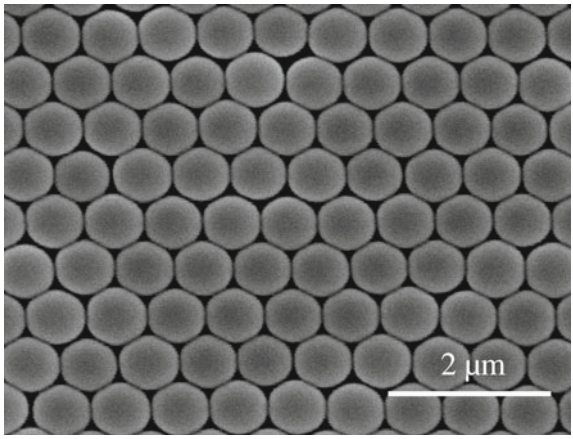


**Fig. 2.19** Scanning electron microscope (SEM) picture of a Ni-coated monolayer of quartz ($a - SiO_2$) microspheres of diameter $d = 0.72\,\mu$m. The support is a 1.0 mm thick $a - SiO_2$ platelet. From Ref. [16]

are used as a lens array allowing single step large area parallel processing [72–76]. Among those are patterns generated from metal-coated monolayers of microspheres by laser-induced forward transfer (LIFT) [77–80].

Through the experiments, close-packed monolayers of amorphous silica ($a - SiO_2$) or polystyrene (PS) microspheres (diameters $d = 0.39, 0.78, 1.0,$ and $1.42\,\mu$m) were deposited on quartz supports (1 mm thick) using colloidal suspensions. The monolayers were covered with different metals (Ag, Au, Ni) and film thickness (30–300 nm) using standard evaporation techniques. A typical metal covered monolayer is shown in Fig. 2.19. The metal films cover approximately the upper half of single spheres, while the lower half remains uncoated. At the top of spheres the thickness of the coating (75 nm) is about equal to that measured with a nearby quartz crystal microbalance (QCM). Towards the edge of spheres the film thickness slightly decreases. In the interstices between the spheres, the coating is placed on the quartz support. Within these areas, the film thickness measured by means of an atomic force microscope (AFM), is equal to that measured by QCM. The areas of close-packed monolayers were, typically, of the order of $\sim cm^2$. Because of certain size dispersion of the microspheres and the deposition technique employed [81], the monolayers exhibit a polycrystalline structure with a typical domain size of about 50–100 m . Transmission experiments were performed at normal incidence both on bare PCSs and on the covered with metal slabs. The transmission measurements were done in the far-field, in a configuration that only collected the zero-order transmission. Since aperture diameters of 1–3 mm were used for the transmission measurements, any polarization dependent effects could not be probed and non-polarized light was used.

**FDTD Modeling**

Simulations were performed by using the FDTD method. A small grid size of 6 nm was used in all reported results. The dielectric constant of the different metals considered were taken from their bulk values, and approximated by a Drude–Lorentz functional form (Table 1.1). Dielectric constants for the quartz support, and the silica and polystyrene microspheres were assumed wavelength independent and set to 1.52, 1.392 and 1.572, respectively. As the geometry of the metal layer is not precisely known, for simplicity the thickness of the metal film on the top of each sphere was assumed to be constant (72 nm). We expect that this simplification of the metal geometry will induce at most some small spectral displacements of the transmission resonances and of the average transmittance, but will otherwise have a negligible effect on the overall transmission properties of the system. In order to compare with the experimental transmittance, only transmission into the zeroth diffraction order was computed.

### *2.5.2 Results and Discussion*

Figure 2.20 compares measured and modeled spectra for silica sphere arrays covered with Ni, Ag and Au metals. Overall, the modeled spectra reproduce quite well the observed features with respect to both the absolute transmission values and peak positions. The main difference that can be observed is the additional peak at around 1300 nm in the calculated spectra. For the case of Ni, this peak seems to be hidden under the shoulder of the main peak. For Ag and Au it seems to be absent in the measured spectra. All peaks in the measured spectra are also slightly broader, likely because of the size-dispersion of the spheres and the polycrystalline structure of the array. Nevertheless, the overall good agreement suggests that this simple fabrication route leads to structures where disorder is small enough as not to spoil the optical transmission resonances expected in perfect arrays.

In the optical regime, the different behavior of the metals is notable. The peaks for Ni are less pronounced, while Ag and Au presents more detailed fine structure in both measured and modeled spectra. This effect is related to the difference in optical properties of these metals. As discussed in Sect. 2.2, Nickel is a less "ideal" metal than Ag and Au, with relatively high absorption in the wavelength region of interest, resulting in less pronounced features in both measured and modeled spectra. The calculated spectra for gold and silver have more defined (and stronger) peaks in comparison to the measured ones at shorter wavelengths. This may be due to the presence of disorder in the sample, where not all unit cells are strictly equal. Also, films deposited onto the microsphere arrays exhibit a poly/nano-crystalline structure, which may alter the optical properties of the metal relative to bulk values used in the calculations. Both such alterations impair resonant behavior, being therefore more evident in Ag and Au than in Ni (where resonances are already hampered by intrinsic absorption of the metal).

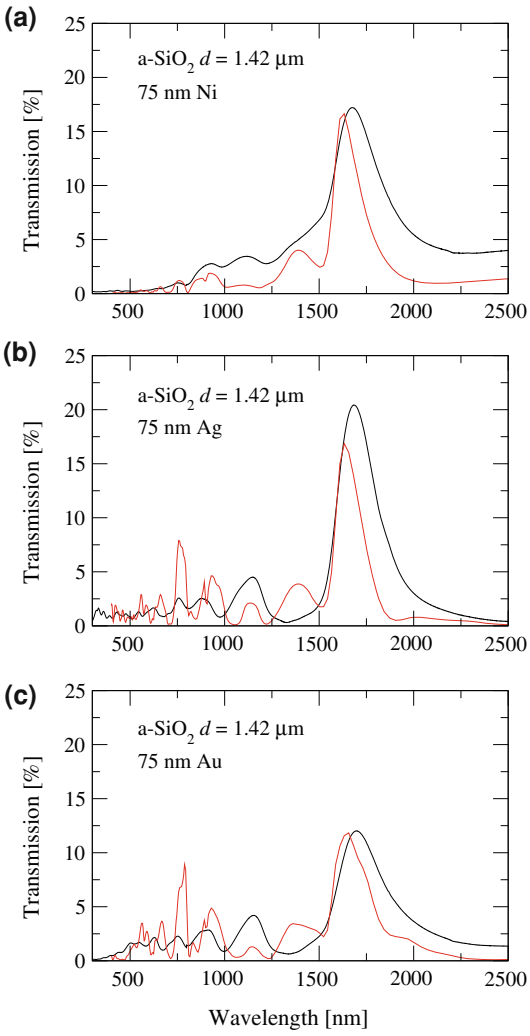


**Fig. 2.20** Measured (*black*) and calculated (*red*) zero order transmission through metal coated MLs of a $-$ $SiO_2$ microspheres ($d = 1.42\,\mu$m). From Ref. [16]

The situation is different in the telecom regime (transmission peaks appearing around 1600 nm in Fig. 2.20). In this case, the transmission level for all metals considered is similar, being even larger for Ni than for Au or Ag. Notice that, in this case, the full-width-at-half-maximum ($\Delta\lambda$) is very very similar for all three metals considered: 163 nm for Ni, 154 nm for Ag and 126 nm for Au. Given that the dielectric constant of Ni is very different from that of Ag and Au, this implies that the time that the electromagnetic field stays at the structure is limited by radiation, more than by absorption. This time can be estimated as $T = \lambda^2_{\max}/(c\Delta\lambda)$ and the distance that the EM field travels on the surface as $L_T = \lambda^2_{\max}/\Delta\lambda$, where $\lambda_{\max}$ is the spectral position of the transmission maximum and $c$ the speed of light. From the

simulation we can estimate $L_T = 16.2\,\mu$m, $17.4\,\mu$m and $12.6\,\mu$m for Ni, Ag and Au, respectively. This values are smaller than, for instance, the propagation lengths of surface plasmon polaritons at $\lambda = 1600$ nm (which approximately are $25\,\mu$m for Ni, $360\,\mu$m for Ag and $360\,\mu$m for Au), which reenforces the hypothesis that radiation losses dominate over absorption. Notice also that the larger absorption in the case of Ni could be compensated by the larger skin depth (33 nm in Ni, 22 nm in Ag and 23 nm in Au for $\lambda \approx 1600$ nm), which implies both a larger direct transmission through the metal layer and a larger effective hole radius.

To further study the behavior of this composite structure and the validity of using the FDTD method, different parameters were investigated. Here, the refractive index of the spheres was changed by considering polystyrene microspheres. The sphere diameters (periodicity) was also altered, see Fig. 2.21. As expected, by using monolayers of polystyrene spheres (with a higher refractive index than a $-\ SiO_2$) with different diameters, one finds that the main peak shifts with the periodicity of the array. Again, measured and modeled spectra show good agreement (Fig. 2.21). We associate the higher values for the calculated peaks both to disorder in the actual sample and to the fact that absorption in the PS spheres was neglected in the calculations.

The main peak is further red-shifted relative to the diameter by about a factor of 1.3 $d$, whereas a factor of 1.2 $d$ was observed for the silica spheres (Fig. 2.20). This is related to the higher refractive index of the polystyrene spheres relative to silica. The same effect is observed for PCS without metal, that is, a higher "effective" refractive index red-shifts the main minima (dip) in transmission [67, 68]. Additionally, the main dip in the dotted curves in Fig. 2.21, that show the transmission of the bare MLs, and the main transmission peak of the metal coated arrays show a clear correlation. The main transmission peak is slightly red-shifted compared to the main dip. This behavior implies that the transmission is related to the supported modes of the bare (uncoated) 2D-PCS as suggested earlier [69]. The transmission spectra of the bare PCSs are also included in the graphs where, once again, the differences in the transmission curves can be seen. The modeled spectra show much narrower main dips than the measured ones, again pointing to the influence of absorption in the PS spheres, and also to size dispersion of spheres and grain boundaries within the monolayers. In any case, the fabrication method allows for simple scaling (positioning) of any transmission peak (or dip) of interest, as can be seen in Fig. 2.21. It is also demonstrated in Fig. 2.21c that the main peak can be easily shifted to the visible wavelength region. This could be interesting with possible application for these composite structures as, e.g., for the fabrication of relatively narrow band filters.

Importantly, the close spectral correspondence between transmission dips in the uncoated system and transmission peaks in the coated one is also present in the calculation, even more clearly so, as spectral features are narrower here than in the experiment. The thickness of the metal deposit was also varied for both Ag and Au metals on silica spheres, see Fig. 2.22. For both metals, the intensity of the main transmission peak decreases roughly exponentially. Notice that the measured transmission is higher for thicker deposits compared to modeled spectra, which we associate to the assumption of homogenous film thickness in the calculations. Again, quite large

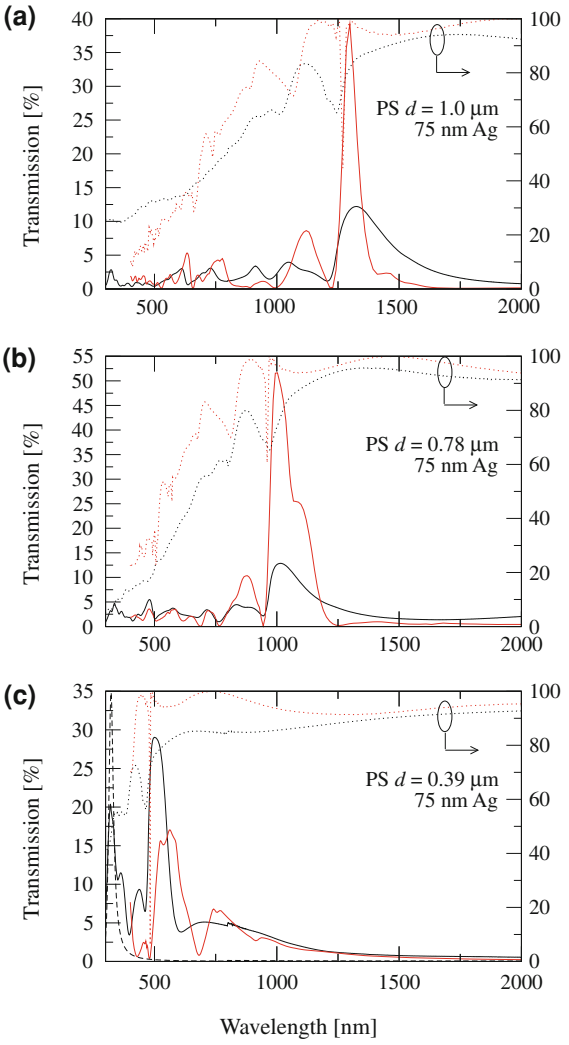


**Fig. 2.21** Measured (*black*) and modeled (*red*) zero order transmission through monolayers of polystyrene spheres. Bare monolayer-dotted curves (*right* y-scales) and coated with 75 nm silver-full curves (*left* y-scales). **a** $d = 1.0\,\mu$m, **b** $d = 0.78\,\mu$m, **c** $d = 0.39\,\mu$m. The main peak (or dip) scales with the periodicity (**d**). From Ref. [16]

discrepancies can be observed between measured and calculated spectra in the short wavelength region. Also, the main peak red shifts as the thickness is increased (More pronounced for the measured spectra). Possibly, this can be related to coupling of the modes on the two interfaces; PCS/metal and metal/air. For films with thickness less than 50 nm, two peaks can be observed in the calculated spectra, whereas only one peak is observed for the thicker deposits, suggesting a coupling/decoupling behavior of the two modes as the thickness is increased.

The rest of the section is devoted to ascertain which are the relevant mechanisms for the transmission resonances in this system. Notice that the composite slab is quite complex, and transmission resonances could be due to one or several factors,

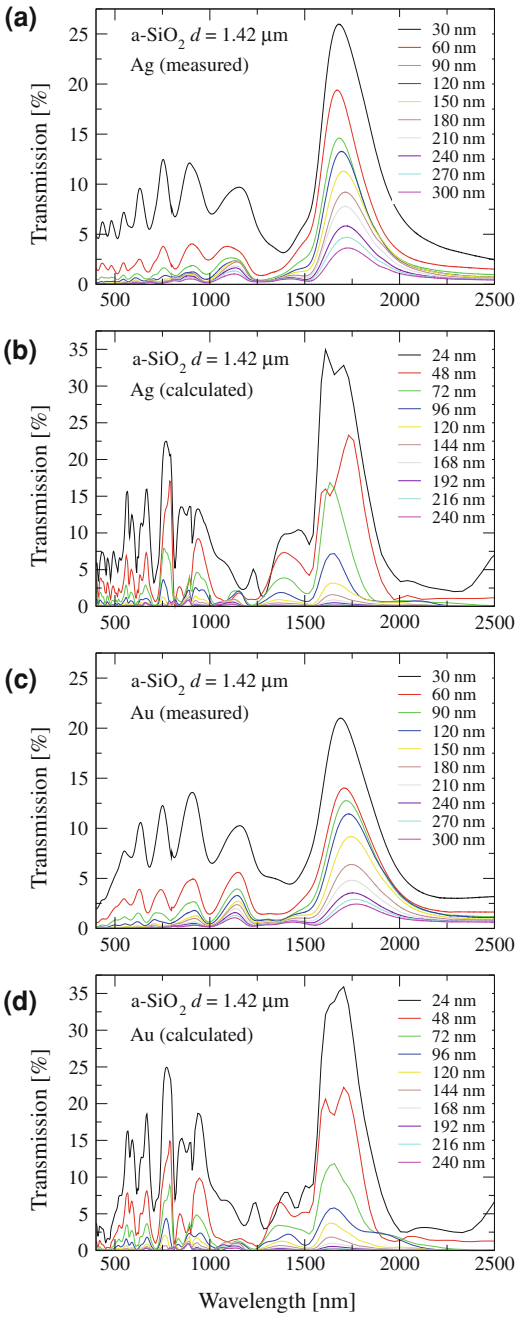


**Fig. 2.22** Measured (**a**, **c**) and calculated (**b**, **d**) transmission spectra for different thicknesses of the metal deposit. Ag and Au were used on $d = 1.42\,\mu$m silica spheres. From Ref. [16].

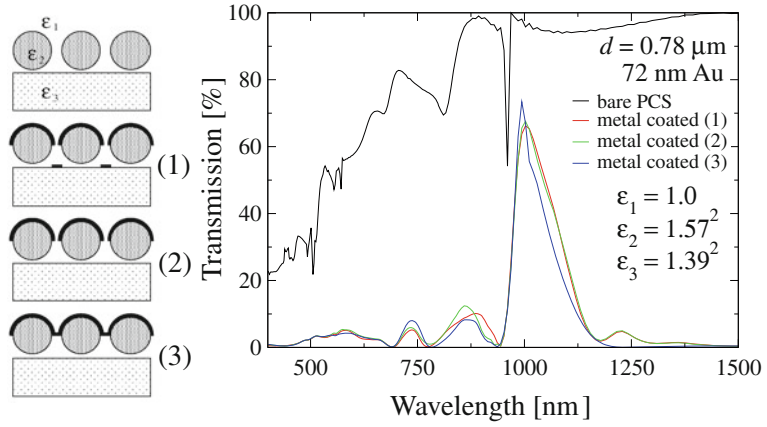


**Fig. 2.23** Calculated transmission curves for bare PCS and with different metal coverage (1)–(3). From Ref. [16].

like: surface plasmons coupled either through the holes in the interstices or through the metal (if the metal film is optically thin), photonic crystal modes in the sphere layer (weakly or strongly coupled), Mie resonances of the spheres, particle plasmon modes of the triangular metal deposit on the quartz support, etc. The good agreement between measured and calculated spectra allows us to study of the relevance of these different mechanisms, through the modeling of similar but simpler systems.

To start with, two different but related structures were modeled: Metal coated sphere arrays without any metal on the support and sphere arrays fully covered with metal (and consequently no metal on the support either). The calculated results are shown in Fig. 2.23. Interestingly, the calculations reveal that the metal deposit on the support has negligible influence on the overall transmission and, more importantly, that the transmission spectra remains practically unaltered if the holey metal cap covering the spheres is replaced by a continuous metal cap. So, for this parameter range, the coupling across the metal film is mainly due to coupling through the metal, and not through the holes. This calculation also shows that there is no need for improvements in the fabrication process in order to get rid of the deposited metal particles in the substrate. In order to investigate the importance of a PCS and its guided modes as support to the metal film, the spheres were simply removed in the model system by introducing a uniform refractive index below the corrugated metal film (both with and without holes). In this case, the transmission process can be explained by a resonant model involving surface plasmon excitations and tunneling through the corrugated thin metal film [4, 37]. The results are depicted in Fig. 2.24. Remarkably, in the uniform dielectric case, absolute transmission values are much lower than those obtained for the sphere system. In addition, we have computed the transmission for a thin planar film with triangular holes (with the same size as those in the experiment) in graphene symmetry. Again transmission values are low when compared with those in the capped sphere system. These findings suggest

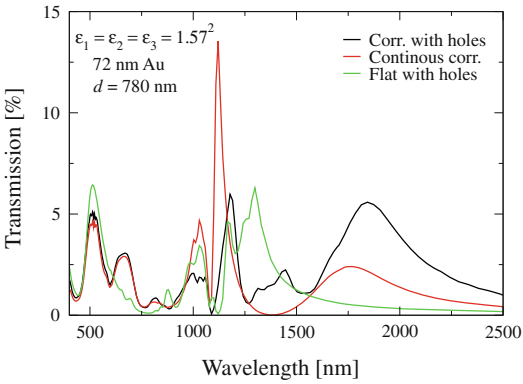


**Fig. 2.24** Calculated transmission curves for corrugated (with and without holes) and planar metal film with holes in a graphene symmetry. All films were modeled in a homogeneous media. The metal considered is Au and the lattice parameter is $d = 780$ nm. From Ref. [16].

that the presence of the photonic crystal layer is of great importance in the overall transmission mechanism. The close spectral correspondence between transmission peaks in the coated case and transmission dips in the uncoated one, already points to the possible relevance of guided modes in the photonic crystal. This relevance is corroborated by the computed electromagnetic field distributions (see Fig. 2.25 for a representative case), which present strong field confinement at the location of the spheres.

It is interesting to highlight the differences on the transmittance between guided modes in a photonic crystal and guided modes in a uniform dielectric slab. The first difference is related to the "energetics". A first estimation of the spectral position at which EOT features appear can be obtained by computing the frequency of the surface mode involved, at a wavevector equal to the shortest reciprocal lattice vector (for the case of normal incidence considered here). Similarly, dips in the corrugated dielectric are expected to appear at the same condition, as Fig. 2.21 shows. Let us start by considering the uniform dielectric slab. The point here is that the guided modes in a vacuum-metal-dielectric film-substrate (VMDS) waveguide are different from the ones in a vacuum-dielectric film-substrate (VDS) configuration, due to the large differences between the Fresnel coefficients for metal/dielectric and metal/air interfaces. Therefore, features in a corrugated dielectric and a corrugated metal, each of them placed on top of dielectric slab, should appear at different wavelengths. To illustrate this point, we have computed the wavelengths of the guided modes in both VMDS and VDS configurations, for the following parameters (motivated by the experimental setup): the dielectric film has a dielectric constant $\varepsilon = 1.57^2$ and a thickness $t = 780$ nm. The substrate has a dielectric constant $\varepsilon = 1.5^2$. The considered wavevector is $k = 2\pi/t$ (in a sphere array the inter-distance between spheres is equal to the dielectric film thickness). The metal thickness is 70 nm and its dielectric constant is taken as $\varepsilon_{\text{metal}} = -50$ (approximately the value for Au at $\lambda \sim 1000$ nm). We obtain that the wavelengths of the guided modes are: 1176 nm for the VDS configuration and 1235 nm for the VMDS case. On the contrary, the dispersion relation of guided modes in the photonic crystal (composed by the two-

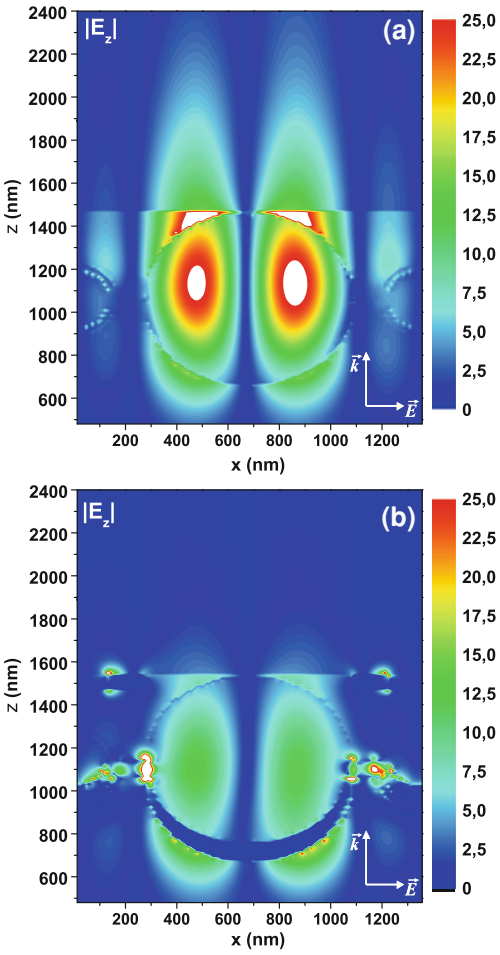


**Fig. 2.25** Contour plots for the modulus of the z-component of the electric field across a plane passing through the center of the spheres. The system under study is the one considered in 2.21. (**b**). **a** uncoated case at the wavelength of the main transmission dip ($\lambda = 944\,\text{nm}$). **b** coated case at the main transmission maximum ($\lambda = 1002\,\text{nm}$). From Ref. [16].

dimensional arrays of dielectric spheres) is weakly affected by the presence of the metal film (calculations not presented here estimate that the difference between the wavelengths of the guided mode in the metal capped and uncapped configurations is of the order of 5 nm). This is so because, in this case, the z-component of the electric field (which is the relevant one for guided modes) is more concentrated close to the center of the spheres (see Fig. 2.25), so a smaller fraction of the field senses the different Fresnel coefficients alluded above.

The second difference is related to the coupling of the light, passing through the metal film in the presence of guided modes, to the different radiation orders. Guided modes in photonic crystals represent a weaker coupling to radiation modes than either guided modes in a dielectric or surface plasmons (again due to the previously cited concentration of the electric field in the photonic crystal guided modes, which places the EM field away from the radiation region). Notice that radiation damping impairs

the resonant transmission process, so this feature of photonic crystal modes explains why the configuration of metal film on top of a photonic crystal is so efficient for EOT phenomena (Compare Figs. 2.23 with 2.24).

It must be noted that we have concentrated on the transmission peak appearing at larger wavelengths. At shorter (optical) wavelengths there is also a close correspondence between transmission dips in the uncoated system and transmission peaks in the coated one, pointing to again to the relevance of guided modes. These modes could be due either to remappings (aided by a reciprocal lattice vector) of the fundamental guided mode or to higher order guided modes. No attempt has been made here to assign a definite origin to these modes as they give rise to small transmission peaks.

## 2.6 Conclusions

In conclusion, we have investigated three different questions that strongly affect EOT: the metal chosen, the metal thickness and the hole shape.

To elucidate about the influence of the metal chosen on EOT we have investigated theoretically the resonant optical transmission through circular hole arrays drilled in different metals. We have performed two series of calculations. In both of them all lengths except the metal thickness are scaled by the same factor. In one of the series the metal thickness is kept fixed, while in the other the metal thickness is also scaled. In the first case, for which there is experimental data available [32], the comparison between experiment and theory is very good. These results confirm that, in the experiments, the effects of possible inhomogeneities in hole shape and size were small. Also the metal surface, despite the processing that has received when creating the holes, is well described by a dielectric constant close to its bulk value. Moreover, FDTD is validated as a predictive tool for this kind of systems, as the comparison with experimental data did not require any fitting parameter. The case in which all lengths were scaled allowed the comparison of the transmission properties of real metals with those of a perfect conductor. The analysis reveals different types of behavior of the transmittance in hole arrays in different sets of metals: in Ag, Au or Cu, the transmittance is even larger than in the perfect conductor case, reflecting that absorption is low and the penetration of EM fields effectively enlarges the hole area. In Ni and Cr, although the effective area is as large as in the previous metals, absorption strongly reduces the resonant transmittance. Aluminum behaves very much like a perfect conductor at the lower wavelength end of the optical regime but for peak wavelengths $\geq$700 nm the resonant transmittance characteristics are dominated by absorption, as in the case of Ni and Cr. Finally, tungsten, which in the spectral range considered is a dielectric, presents transmission resonances with maxima much smaller than those of even the worse metals (Ni, Cr).

In the study of EOT when the film thickness is varied, we have shown that the EOT peak can be tuned to longer wavelengths (by even hundreds of nm) by decreasing the film thickness without strongly affecting neither transmission intensity nor peak

visibility (which is still large at $w \sim 20$ nm). We have demonstrated that only SRs modes are responsible for the EOT phenomenon in optically thin metallic 2DHAs. This may be of interest in the fields of EOT and Negative Refractive Index (which has been obtained in stacked optically thin 2DHAs [82]).

From our study on the hole shape dependence of EOT, we have explained theoretically the interplay between two different mechanisms that enhance the transmission of light through 2D arrays of rectangular holes: SPP-based extraordinary transmission and enhanced transmission assisted by the excitation of a localized resonance, spectrally located at the cut-off wavelength of the hole waveguide, $\lambda_c$. We have shown that when $d < \lambda_c$ the transmission resonance has a localized nature mainly, i.e. it is mainly governed by the behavior of a single hole. In contrast, for $d > \lambda_c$, SPP governs the transmittance through the structure, We have also demonstrated that in this last case, resonant transmission is mainly limited by the absorption in the metal.

Finally, the 2D-photonic crystal structure composed by periodically arranged microspheres and covered with thin metal films, has been found to present EOT. Measured spectra have been compared with spectra calculated with FDTD and the good agreement has allowed modeling of slightly modified structures to get further information about possible transmission mechanisms. The calculations indicate that the guided modes in the PCS are mainly responsible to the relatively large transmission values observed (especially for the main peak). In contrast, the small holes in the thin metal film (at the interstices between three adjacent spheres) and metal deposit onto the support do not strongly influence the main transmission peak. The high transmission values, straightforward fabrication and easy up-scaling of the metal covered slabs together with simple peak positioning in a broad wavelength region (VIS/IR) make these structures a good candidate for application purposes.

## References

1. H.A. Bethe, Phys. Rev. **66**, 163 (1944)
2. T.W. Ebbesen, H.L. Lezec, H.F. Ghaemi, T. Thio, P.A. Wolff, Nature **391**, 667 (1998)
3. H.F. Ghaemi, T. Thio, D.E. Grupp, T.W. Ebbesen, H.J. Lezec, Phys. Rev. B **58**, 6779 (1998)
4. L. Martín-Moreno, F.J. García-Vidal, H.J. Lezec, K.M. Pellerin, T. Thio, J.B. Pendry, T.W. Ebbesen, Phys. Rev. Lett. **86**, 1114 (2001)
5. L. Martín-Moreno, F.J. García-Vidal, Opt. Express **12**, 3619 (2004)
6. C. Genet, T.W. Ebbesen, Nature **445**, 39 (2007)
7. D.E. Grupp, H.J. Lezec, T.W. Ebbesen, K.M. Pellerin, T. Thio, Appl. Phys. Lett. **77**, 1569 (2000)
8. Q. Wang, J. Li, C. Huang, C. Zhang, Y. Zhu, Appl. Phys. Lett. **87**, 091105 (2005)
9. J.R. Krenn, A. Dereux, J.C. Weeber, E. Bourillot, Y. Lacroute, J.P. Goudonnet, G. Schider, W. Gotschy, A. Leitner, F.R. Aussenegg et al., Phys. Rev. Lett. **82**, 2590 (1999)
10. H.J. Lezec, A. Degiron, E. Devaux, R.A. Linke, L. Martín-Moreno, F.J. García-Vidal, T.W. Ebbesen, Science **297**, 820 (2002)
11. de F.J.G. Abajo, Rev. Mod. Phys. **79**, 1267 (2007)
12. F. J. Garcia-Vidal, L. Martin-Moreno, T. W. Ebbesen, and L. K. Kuipers, Rev. Mod. Phys. (2009), (To be published).
13. S.G. Rodrigo, F. J. García-Vidal, L. Martín-Moreno, Phys. Rev. B **77**, 075401 (2008)

14. S.G. Rodrigo, L. Martín-Moreno, A.Y. Nikitin, A.V. Kats, I.S. Spevak, F.J. García-Vidal, Opt. Lett. **34**, 4 (2009)
15. A. Mary, S.G. Rodrigo, L. Martín-Moreno, F.J. García-Vidal, Phys. Rev. B **76**, 195414 (2007)
16. L. Landström, D. Brodoceanu, D. Bäuerle, F.J. Garcia-Vidal, S.G. Rodrigo, L. Martin-Moreno, Opt. Express **17**, 761 (2009)
17. L. Salomon, F.D. Grillot, A.V. Zayats, de F. Fornel, Phys. Rev. Lett. **86**, 1110 (2001)
18. P. Lalanne, J.C. Rodier, J.P. Hugonin, J. Opt. A: Pure Appl. Opt. **7**, 422 (2005)
19. C. Genet, van M.P. Exter, J.P. Woerdman, Opt. Commun. **225**, 331 (2003)
20. M. Sarrazin, J.-P. Vigneron, Phys. Rev. E **68**, 016603 (2003)
21. E. Moreno, L. Martín-Moreno, F.J. García-Vidal, J. Opt. A: Pure Appl. Opt. **8**, S94 (2006)
22. E. Moreno, F.J. García-Vidal, L. Martín-Moreno, Phys. Rev. B. **69**, 121402(R) (2004)
23. B. Wang, W. Dai, A. Fang, L. Zhang, G. Tuttle, T. Koschny, C.M. Soukoulis, Phys. Rev. B **74**, 195104 (2006)
24. E. Dulkeith, S.J. McNab, Y.A. Vlasov, Phys. Rev. B **72**, 115102 (2005)
25. J. Christensen, A.I. Fernández-Domínguez, de F. León-Pérez, L. Martín- Moreno, F.J. García-Vidal, Nature Phys. **3**, 851 (2007)
26. E. Moreno, A.I. Fernández-Domínguez, J.I. Cirac, F.J. García-Vidal, L. Martín-Moreno, Phys. Rev. Lett. **95**, 170406 (2005)
27. R. Gordon, A.G. Brolo, A. McKinnon, A. Rajora, B. Leathem, K.L. Kavanagh, Phys. Rev. Lett. **92**, 037401 (2004)
28. K.J.K. Koerkamp, S. Enoch, F.B. Segerink, van N.F. Hulst, L. Kuipers, Phys. Rev. Lett. **92**, 183901 (2004)
29. A. Degiron, T.W. Ebbesen, J. Opt. A: Pure Appl. Opt. **7**, S90 (2005)
30. A. Degiron, H.J. Lezec, N. Yamamoto, T.W. Ebbesen, Opt. Commun. **239**, 61 (2004)
31. F.J. García-Vidal, E. Moreno, J.A. Porto, L. Martín-Moreno, Phys. Rev. Lett. **95**, 103901 (2005)
32. F. Przybilla, A. Degiron, J.-Y. Laluet, C. Genet, T.W. Ebbesen, J. Opt. A: Pure Appl. Opt. **8**, 458 (2006)
33. A. Vial, A.-S. Grimault, D. Macías, D. Barchiesi, de la M.L. Chapelle, Phys. Rev. B **71**, 085416 (2005)
34. A.D. Rakić, A.B. Djurišić, J.M. Elazar, M.L. Majewski, Appl. Opt. **37**, 22 (1998)
35. E.D. Palik, *Handbook of optical constants of solids* ed. by Palik, D. Edward (Academic Press, New York, 1985)
36. E.D. Palik, *Handbook of optical constants of solids II* ed. by Palik, D. Edward (Academic Press, Boston, 1991).
37. A. Krishnan, T. Thio, T.J. Kim, H.L. Lezec, T.W. Ebbesen, P.A. Wolff, J.B. Pendry, L. Martín-Moreno, F.J. García-Vidal, Opt. Commun. **200**, 1 (2001)
38. J.B. Pendry, L. Martín-Moreno, F.J. García-Vidal, Science **305**(5685), 847 (2004)
39. F.J. García-Vidal, L. Martín-Moreno, J.B. Pendry, J. Opt. A: Pure Appl. Opt. **7**, S97 (2005)
40. de F.J.G. Abajo, J.J. Saenz, Phys. Rev. Lett. **95**, 233901 (2005)
41. J. Bravo-Abad, F.J. García-Vidal, L. Martín-Moreno, Phys. Rev. Lett. **93**, 227401 (2004)
42. F.J. García-Vidal, L. Martín-Moreno, E. Moreno, .K.S. Kumar, R. Gordon, Phys. Rev. B **74**, 153411 (2006)
43. M. Sarrazin, J.-P. Vigneron, Phys. Rev. B **71**, 075404 (2005)
44. I.R. Hooper, J.R. Sambles, Phys. Rev. B **70**, 045421 (2004)
45. D. Gérard, L. Salomon, de F. Fornel, A.V. Zayats, Opt. Express **12**, 3652 (2004)
46. E.N. Economou, Phys. Rev. **182**, 539 (1969)
47. A. Azad, W. Zhang, Opt. Lett. **30**, 2945 (2005)
48. X. Shou, A. Agrawal, A. Nahata, Opt. Express **13**, 9834 (2005)
49. Q. Cao, P. Lalanne, Phys. Rev. Lett. **88**, 057403 (2002)
50. S.A. Darmanyan, A.V. Zayats, Phys. Rev. B **67**, 035424 (2003)
51. A.V. Kats, M.L. Nesterov, A.Y. Nikitin, Phys. Rev. B **76**, 045413 (2007)
52. H. Cao, A. Nahata, Opt. Express **12**, 3664 (2004)

53. van der K.L. Molen, K.J.K. Koerkamp, S. Enoch, F.B. Segerink, van N.F. Hulst, L. Kuipers, Phys. Rev. B **72**, 045421 (2005)
54. Z. Ruan, M. Qiu, Phys. Rev. Lett. **96**, 233901 (2006)
55. R. Gordon, A. Brolo, Opt. Express **13**, 1933 (2005)
56. W. Jia, X. Liu, Eur. Phys. J. B **46**, 343 (2005)
57. T. López-Rios, D. Mendoza, F.J. García-Vidal, J. Sánchez-Dehesa, B. Pannetier, Phys. Rev. Lett. **81**, 665 (1998)
58. D. Crouse, M. Arend, J. Zou, P. Keshavareddy, Opt. Express **14**, 2047 (2006)
59. D.C. Skigin, R.A. Depine, Phys. Rev. E **63**, 046608 (2001)
60. de F.J.G. Abajo, R. Gómez-Medina, J.J. Sáenz, Phys. Rev. E **72**, 016608 (2005)
61. D.E. Grupp, H. Lezec, T. Thio, T. Ebbesen, Adv. Mater. **11**, 860 (1999)
62. Y.-H. Ye, J.-Y. Zhang, Appl. Phys. Lett. **84**, 2977 (2004)
63. van der K.L. Molen, F.B. Segerink, van N.F. Hulst, L. Kuipers, Appl. Phys. Lett. **85**, 4316 (2004)
64. D. Qu, D. Grischkowsky, Phys. Rev. Lett. **93**, 196804 (2004)
65. C. Janke, J.G. Rivas, C. Schotsch, L. Beckmann, P.H. Bolivar, H. Kurz, Phys. Rev. B **69**, 205314 (2004)
66. W.L. Barnes, W.A. Murray, J. Dintinger, E. Devaux, T. Ebbesen, Phys. Rev. Lett. **92**, 107401 (2004)
67. L. Landström, D. Brodoceanu, N. Arnold, K. Piglmayer, D. Bäuerle, Appl. Phys. A **81**, 911 (2005)
68. L. Landström, N. Arnold, D. Brodoceanu, K. Piglmayer, D. Bäuerle, Appl. Phys. A **83**, 271 (2006)
69. L. Landström, D. Brodoceanu, K. Piglmayer, D. Bäuerle, Appl. Phys. A **84**, 373 (2006)
70. L. Collot, V. Lefevre-Seguin, M. Brune, J. Raimond, S. Haroche, Europhys. Lett. **23**, 327 (1993)
71. M.-H. Wu, G.M. Whitesides, Appl. Phys. Lett. **78**, 2273 (2001)
72. D. Bäuerle, T. Gumpenberger, D. Brodoceanu, G. Langer, J. Kofler, J. Heitz, K. Piglmayer, in *Laser Cleaning II*, ed. by D.M. Kane (World Scientific, Singapore, 2005).
73. D. Bäuerle, G. Wysocki, L. Landström, J. Klimstein, K. Piglmayer, J. Heitz, Proc. SPIE **5063**, 8 (2003)
74. K. Piglmayer, R. Denk, D. Bäuerle, Appl. Phys. Lett. **80**, 4693 (2002)
75. G. Wysocki, R. Denk, K. Piglmayer, N. Arnold, D. Bäuerle, Appl. Phys. Lett. **82**, 92 (2003)
76. D. Bäuerle, K. Piglmayer, R. Denk, N. Arnold, Lambda Highlights **60**, 1 (2002)
77. D. Bäuerle, *Laser Processing and Chemistry*, 3rd edn. (Springer, Berlin, 2000)
78. L. Landström, J. Klimstein, G. Schrems, K. Piglmayer, D. Bäuerle, Appl. Phys. A **78**, 537 (2004)
79. G. Langer, D. Brodoceanu, D. Bäuerle, Appl. Phys. Lett. **89**, 261104 (2006)
80. A. Pikulin, N. Bityurin, D. Brodoceanu, G. Langer, D. Bäuerle, Appl. Phys. Lett. **91**, 191106 (2007)
81. R. Micheletto, H. Fukuda, M. Ohtsu, Langmuir **11**, 3333 (1995)
82. S. Zhang, W. Fan, N.C. Panoiu, R.M. Osgood, S.R.J. Brueck, Phys. Rev. Lett. **95**, 137404 (2005)

http://www.springer.com/978-3-642-23084-4

Optical Properties of Nanostructured Metallic Systems
Studied with the Finite-Difference Time-Domain Method

Rodrigo, S.G.

2012, XX, 163 p. 95 illus., 9 illus. in color., Hardcover
ISBN: 978-3-642-23084-4